

Experiments with Schrödinger Cellular Automata

Kees van Berkel, Jan de Graaf, and Kees van Hee

TU Eindhoven, Dept. of Mathematics & Computer Science, P.O. Box 513, 5600 MB Eindhoven, The Netherlands

We derive a class of cellular automata for the Schrödinger Hamiltonian, including scalar and vector potentials. It is based on a multi-split of the Hamiltonian, resulting in a multi-step unitary evolution operator in discrete time and space. Experiments with one-dimensional automata offer quantitative insight in phase and group velocities, energy levels, related approximation errors, and the evolution of a time-dependent harmonic oscillator. The apparent effects of spatial waveform aliasing are intriguing. Interference experiments with two-dimensional automata include refraction, Davisson-Germer, Mach-Zehnder, single & double slit, and Aharonov-Bohm.

Keywords: Schrödinger equation, cellular automata, time-dependent harmonic oscillator, interference, Davisson-Germer, Mach-Zehnder, double-slit, Aharonov-Bohm.

1 Introduction

The Schrödinger equation is a linear partial differential equation that governs the non-relativistic evolution of the wave function of a quantum-mechanical system. For a single particle it has the form [22], Vol. III, 21-1

$$\begin{aligned} i\hbar \frac{\partial \Psi(\mathbf{x}, t)}{\partial t} &= \mathcal{H} \Psi(\mathbf{x}, t) \\ \mathcal{H} &= \frac{1}{2m} \left(\frac{\hbar}{i} \nabla - q\mathbf{A}(\mathbf{x}) \right) \cdot \left(\frac{\hbar}{i} \nabla - q\mathbf{A}(\mathbf{x}) \right) + q\phi(\mathbf{x}) , \end{aligned} \quad (1.1)$$

where $\Psi(\mathbf{x}, t)$ is the three-dimensional wave function, \mathcal{H} is the so-called Hamiltonian (operator), and \hbar the Planck constant. In addition, m denotes the particle's mass, q the particle's charge, $\mathbf{A}(\mathbf{x})$ the vector potential and $\phi(\mathbf{x})$ the scalar potential. The Hamiltonian is time-independent since neither $\phi(\mathbf{x})$ nor $\mathbf{A}(\mathbf{x})$ depend on time. Usually the vector potential $\mathbf{A}(\mathbf{x})$ is not considered, resulting in a simpler version of the Hamiltonian.

$$\mathcal{H} = -\frac{\hbar^2}{2m} \nabla^2 + V(\mathbf{x}) , \quad (1.2)$$

Kees van Berkel: c.h.v.berkel@tue.nl

Jan de Graaf: passed away on 2024, September 16.

Kees van Hee: k.m.v.hee@tue.nl

where $V(\mathbf{x}) = q\phi(\mathbf{x})$ is the potential(-energy) function. For a free particle, $V(\mathbf{x}) = 0$ and the Hamiltonian further reduces to

$$\mathcal{H} = -\frac{\hbar^2}{2m}\nabla^2. \quad (1.3)$$

Textbooks such as [24] present analytical solutions for a variety of simple quantum systems. For systems with non-trivial $V(\mathbf{x})$ or $\mathbf{A}(\mathbf{x})$ numerical techniques can be used to approximate the continuous solution of Ψ in discrete time and space. This paper explores the opposite perspective: what if the Schrödinger equation is a continuous approximation of a discrete universe? *What if*, e.g. at the Planck scale, quantum dynamics occurs on a discrete lattice and in discrete time steps, as for example in [39, 23, 17, 7, 10]? For this exploration cellular automata are used as a tool. Quoting [40]:

Cellular automata are discrete dynamical systems whose behavior is completely specified in terms of a local relation, much as is the case for a large class of continuous dynamical systems defined by partial differential equations. *In this sense, cellular automata are the computer scientist’s counterpart to the physicist’s concept of “field.”*

The Schrödinger cellular automata (SCA) consist of a finite number, N , of cells, where the state of each cell is a complex number representing the value of the wave function at that location. The automata are linear and the update rule (“local relation” in the quote above) can therefore be represented by an $N \times N$ evolution matrix \mathbf{U} . Matrix \mathbf{U} must be both *unitary*, to preserve Born probability, and *local* to meet the locality requirement of cellular automata. For a 1D SCA this locality means that \mathbf{U} must be band-structured.

1.1 Contributions

The contributions of this work include the following.

1. A systematic derivation of an evolution matrix \mathbf{U} for the 3D Schrödinger Hamiltonian (1.1) that is both local and unitary, with $\mathcal{O}(\tau^3)$ error for time step τ . (Section 2.)
2. A derivation of the phase velocity, group velocity, and dispersion relation, as well as the energy levels of the infinite potential well and the harmonic oscillator. These include analytic expressions for the \mathbf{U} -approximation error, and descriptions of aliasing effects resulting from space discretization. (Section 3.)
3. Experiments with SCA describing a time-dependent harmonic oscillator, including adiabatic heating (Subsection 3.6), 2D reflection and refraction, the Davisson-Germer experiment, the Mach-Zehnder interferometer, the single and double-slit experiments, and two variants of the Aharonov-Bohm effect. (Section 4.)

The Python code for the SCA experiments is available on github [42] and the animations can be viewed on youtube [43].

1.2 Related work

Numerical techniques can be applied to solve the Schrödinger equation, typically based on the Crank-Nicolson method [16]. Mena [31], amongst others, applied this method to various systems, including the double-slit experiment based a 2D grid of $N = 160 \times 160$ cells. The

evolution matrix \mathbf{U} combines forward Euler and backward Euler integration, and is therefore dense, with all its elements nonzero. This non-locality is incompatible with cellular automata and also implies a very high computational load.

Schrödinger CA were pioneered by Grössing and Zeilinger [25]. However, their evolution matrix \mathbf{U} is not unitary, which introduces a need for periodic normalization. Meyer [33] identified a class of cellular automata where \mathbf{U} is both unitary and band structured, based on the work of Toffoli [40] on so-called *partitioned cellular automata*. Boghosian and Taylor [11] propose a first SCA and showed that in the continuum limit it obeys the Schrödinger equation. In Section 2.2 we derive essentially the same SCA. They also discuss the addition of an external (scalar) potential and offer a dispersion relation.

Dirac cellular automata (DCA) are cellular automata based on the Dirac equation, as proposed by Bialynicki-Birula [8]. D’Ariano [17] extended this work, where he described matrix \mathbf{U} as a quantum circuit. This circuits “consist of alternate uniform rows of gates” inspired by partitioned CA. Bisio et al [9] derive the phase/group velocities for DCA, not addressing periodicity in k or aliasing. See also Costa [15] for background and Arrighi [6] and Farrelly [21] for review articles on the broad area of quantum cellular automata.

Quantum walks (QW) is an extensive field of research related to quantum cellular automata and was pioneered by Aharonov et al [3]. These quantum walks can also be modelled by a unitary matrix \mathbf{U} , where the state and evolution are represented in a different way, based on the notion of a “quantum coin”. Ambainis et al [4] describe a specific class of quantum walks as “an alternation of coin flip and moving step”, adopting the two-step CA approach of [33]. Both alternate QWs (AQW, Bru et al [12]), and staggered QWs (Portugal et al [36]) are based on this two-step approach, with Strauch [38] describing a first Schrödinger QW. Generalization to 3+1 dimensions are addressed by Arrighi et al [7] and by D’Ariano et al [20]. Costa et al [14] offer a translation of staggered QW to partitioned unitary quantum CAs (PUQCA). Jolly et al [27] introduce *twisted* PQWs (Plastic Quantum Walkers), which adds a dispersion term (“twist”) to a class SQW/PQW that admits a continuum limit (“plasticity”). Our evolution operator \mathbf{U} is explicitly dependent on τ and has the continuum limit built-in. Subsection 2.6 describes the relation between Schrödinger QWs and Schrödinger CAs.

Adding **vector potential** $\mathbf{A}(\mathbf{x})$ to the Hamiltonian has been explored for quantum walks. For the Dirac Hamiltonian this includes work by Di Molfetta et al [19] in 1 spatial dimension, Arnault et al [5] for a constant and uniform magnetic field, and Martin et al [29] in 2 spatial dimensions. Cedzich et al [13] offer a general framework vector potentials in QWs and apply it to the Hadamard coin. This work adds the vector potential to SCAs in three spatial dimensions, and applies the result to two variants of the Aharonov-Bohm experiment, viz. Mach-Zehnder and double-slit.

Approximation of some form is needed to compute $\exp(i(\mathbf{A} + \mathbf{B})\Delta t)$ in the case that matrices \mathbf{A} and \mathbf{B} do not commute. This unavoidably introduces an approximation error, which commonly is measured as the spectral norm error [37]. Morales et al [34] propose an eigenvalue error, related to the eigenvalues of the underlying Hamiltonian, which allows a clear interpretation for long-time evolutions. In Section 3 the approximation error is measured in terms of phase/group velocities and energy levels.

Experiments with Schrödinger or Dirac versions of CAs or QWs are comparatively rare compared to the extensive work on formalization and mathematical foundations. Furthermore, these experiments are typically limited to one dimension, as e.g. in [9]. A notable exceptions is the 3D Dirac QW of [20]. Oliveira et al [35] describe both single-slit and double-slit experiments based on QWs, where they apply Hadamard, Fourier, and Grover coins, without

reference to the Schrödinger or Dirac equations.

2 Schrödinger Cellular Automata

This section describes the construction of Schrödinger cellular automata in a number of steps: 1) derive a discrete version of the 1D Schrödinger Hamiltonian for a free particle, 2) derive a unitary evolution matrix that is band structured by splitting the 1D Hamiltonian, 3) generalize to 3D for the free particle 4) include the scalar potential $V(\mathbf{x})$ and vector potential $\mathbf{A}(\mathbf{x})$, and 5) include reflector cells to support boundary conditions.

2.1 A discrete Schrödinger Hamiltonian for a free particle

For a one-dimensional cellular automaton with cell size a , a discrete-space version of the Schrödinger Hamiltonian (1.3) becomes

$$\mathbf{H}\Psi(x, t) = -\frac{\hbar^2}{2m} \frac{1}{a^2} (\Psi(x-1, t) - 2\Psi(x, t) + \Psi(x+1, t)) , \quad (2.1)$$

where spatial coordinate x is now integer valued. Hamiltonian \mathbf{H} , assuming periodic boundary conditions, can be represented by a two-dimensional circulant matrix. For $N=8$ cells

$$\begin{aligned} \mathbf{H} &= \delta_m \hat{\mathbf{H}} , \\ \delta_m &= \frac{\hbar^2}{2m} \frac{1}{a^2} , \end{aligned} \quad \hat{\mathbf{H}} = \begin{bmatrix} 2 & -1 & 0 & 0 & 0 & 0 & 0 & -1 \\ -1 & 2 & -1 & 0 & 0 & 0 & 0 & 0 \\ 0 & -1 & 2 & -1 & 0 & 0 & 0 & 0 \\ 0 & 0 & -1 & 2 & -1 & 0 & 0 & 0 \\ 0 & 0 & 0 & -1 & 2 & -1 & 0 & 0 \\ 0 & 0 & 0 & 0 & -1 & 2 & -1 & 0 \\ 0 & 0 & 0 & 0 & 0 & -1 & 2 & -1 \\ -1 & 0 & 0 & 0 & 0 & 0 & -1 & 2 \end{bmatrix} . \quad (2.2)$$

The time evolution of a system is commonly described by ¹

$$|\Psi(t)\rangle = \underline{\mathbf{U}}(t) |\Psi(0)\rangle , \quad \text{with} \quad \underline{\mathbf{U}}(t) = \exp\left(-i\frac{1}{\hbar}\mathbf{H}t\right) . \quad (2.3)$$

Matrix $\underline{\mathbf{U}}$ is a dense matrix: all its elements are nonzero. The discrete-time evolution for *integer* time t , $0 \leq t$, and fixed time step τ thus becomes

$$|\Psi((t+1)\tau)\rangle = \underline{\mathbf{U}} |\Psi(t\tau)\rangle , \quad (2.4)$$

where

$$\underline{\mathbf{U}} = \exp\left(-i\frac{\tau}{\hbar}\mathbf{H}\right) = \exp(-i\theta\hat{\mathbf{H}}) , \quad \text{with} \quad \theta = \frac{\tau}{\hbar}\delta_m = \frac{\hbar}{2m} \frac{\tau}{a^2} . \quad (2.5)$$

Constant θ is dimensionless, and can be seen as a rotation angle. The probability of finding the particle in cell x at time t , denoted by $P(x, t)$, is given by Born's rule:

$$P(x, t) = |\Psi(x, t)|^2 , \quad P(t) = \sum_x P(x, t) = 1 . \quad (2.6)$$

¹Henceforth, $\underline{\mathbf{U}}$ denotes a dense evolution matrix and \mathbf{U} an “SCA-sparse” one.

Grössing and Zeilinger [25] base their SCA on Hamiltonian $\delta_m(\hat{\mathbf{H}} - 2\mathbf{I})$ and approximate the evolution operator by using only the first-order term of its expansion

$$\mathbf{U} = \mathbf{I} - i\theta(\hat{\mathbf{H}} - 2\mathbf{I}) \approx \exp(-i\theta(\hat{\mathbf{H}} - 2\mathbf{I})) . \quad (2.7)$$

Matrix \mathbf{U} is a three-band matrix, which nicely agrees with the locality requirement for a cellular automaton: the value of $\Psi(x, t+1)$ only depends on $\Psi(u, t)$, with u an element of the local neighborhood of x , that is, $u \in \{x-1, x, x+1\}$. This locality comes at a price: matrix \mathbf{U} is *not* unitary, and the overall probability $P(t)$ is therefore not preserved. In practice, this implies the need for an ad-hoc scale factor and regular normalization.

2.2 Split Hamiltonian

Next we derive an evolution matrix \mathbf{U} that is *both* unitary (as required by quantum mechanics), and band structured (as required for cellular automata). As a first step, Hamiltonian $\hat{\mathbf{H}}$ is split into two 2×2 -block diagonal matrices $\hat{\mathbf{H}}_0$ and $\hat{\mathbf{H}}_1$, such that $\hat{\mathbf{H}} = \hat{\mathbf{H}}_0 + \hat{\mathbf{H}}_1$, where

$$\hat{\mathbf{H}}_0 = \mathbf{I}_M \otimes \mathbf{B} , \quad \hat{\mathbf{H}}_1 = \mathbf{S}^{-1} \hat{\mathbf{H}}_0 \mathbf{S} , \quad \mathbf{B} = \begin{bmatrix} 1 & -1 \\ -1 & 1 \end{bmatrix} . \quad (2.8)$$

Here \otimes denotes the Kronecker matrix product, integer M satisfies $2M = N$, and matrix \mathbf{S} is the so-called *circular shift* matrix. The product $\mathbf{S} \mathbf{A}$ yields a specific permutation of matrix \mathbf{A} , with all rows of \mathbf{A} shifted down by one row and with the last row moved to the first position. Below the result of this split for $N=8$ cells.

$$\hat{\mathbf{H}}_0 = \begin{bmatrix} 1 & -1 & 0 & 0 & 0 & 0 & 0 & 0 \\ -1 & 1 & 0 & 0 & 0 & 0 & 0 & 0 \\ 0 & 0 & 1 & -1 & 0 & 0 & 0 & 0 \\ 0 & 0 & -1 & 1 & 0 & 0 & 0 & 0 \\ 0 & 0 & 0 & 0 & 1 & -1 & 0 & 0 \\ 0 & 0 & 0 & 0 & -1 & 1 & 0 & 0 \\ 0 & 0 & 0 & 0 & 0 & 0 & 1 & -1 \\ 0 & 0 & 0 & 0 & 0 & 0 & -1 & 1 \end{bmatrix} \quad \hat{\mathbf{H}}_1 = \begin{bmatrix} 1 & 0 & 0 & 0 & 0 & 0 & 0 & -1 \\ 0 & 1 & -1 & 0 & 0 & 0 & 0 & 0 \\ 0 & -1 & 1 & 0 & 0 & 0 & 0 & 0 \\ 0 & 0 & 0 & 1 & -1 & 0 & 0 & 0 \\ 0 & 0 & 0 & -1 & 1 & 0 & 0 & 0 \\ 0 & 0 & 0 & 0 & 0 & 1 & -1 & 0 \\ 0 & 0 & 0 & 0 & 0 & -1 & 1 & 0 \\ -1 & 0 & 0 & 0 & 0 & 0 & 0 & 1 \end{bmatrix} . \quad (2.9)$$

As matrices $\hat{\mathbf{H}}_0$ and $\hat{\mathbf{H}}_1$ do not commute, the evolution operator can be approximated

$$\begin{aligned} \exp(-i\theta\hat{\mathbf{H}}) &= \exp(-i\theta(\hat{\mathbf{H}}_0 + \hat{\mathbf{H}}_1)) \\ &= \exp(-i\theta\hat{\mathbf{H}}_1) \exp(-i\theta\hat{\mathbf{H}}_0) + \mathcal{O}(\theta^2) \\ &= \mathbf{U} + \mathcal{O}(\theta^2) \\ \mathbf{U} &= \mathbf{U}_1 \mathbf{U}_0 \\ \mathbf{U}_0 &= \exp(-i\theta\hat{\mathbf{H}}_0) = \mathbf{I}_M \otimes \mathbf{C} \\ \mathbf{U}_1 &= \exp(-i\theta\hat{\mathbf{H}}_1) = \mathbf{S}^{-1} \mathbf{U}_0 \mathbf{S} \\ \mathbf{C} &= \exp(-i\theta\mathbf{B}) = \exp(-i\theta) \begin{bmatrix} \cos(\theta) & i \sin(\theta) \\ i \sin(\theta) & \cos(\theta) \end{bmatrix} . \end{aligned} \quad (2.10)$$

Matrices \mathbf{U}_0 and \mathbf{U}_1 are both unitary and have a three-diagonal structure.² For $N=8$

$$\mathbf{U}_1 = \exp(-i\theta) \times \begin{bmatrix} \cos(\theta) & 0 & 0 & 0 & 0 & 0 & 0 & i \sin(\theta) \\ 0 & \cos(\theta) & i \sin(\theta) & 0 & 0 & 0 & 0 & 0 \\ 0 & i \sin(\theta) & \cos(\theta) & 0 & 0 & 0 & 0 & 0 \\ 0 & 0 & 0 & \cos(\theta) & i \sin(\theta) & 0 & 0 & 0 \\ 0 & 0 & 0 & i \sin(\theta) & \cos(\theta) & 0 & 0 & 0 \\ 0 & 0 & 0 & 0 & 0 & \cos(\theta) & i \sin(\theta) & 0 \\ 0 & 0 & 0 & 0 & 0 & i \sin(\theta) & \cos(\theta) & 0 \\ i \sin(\theta) & 0 & 0 & 0 & 0 & 0 & 0 & \cos(\theta) \end{bmatrix} \quad (2.11)$$

Matrix \mathbf{U} is unitary and has a five-diagonal structure.³ For $N=8$

$$\mathbf{U} = \exp(-2i\theta) \times \begin{bmatrix} \cos^2(\theta) & \frac{i \sin(2\theta)}{2} & 0 & 0 & 0 & 0 & -\sin^2(\theta) & \frac{i \sin(2\theta)}{2} \\ \frac{i \sin(2\theta)}{2} & \cos^2(\theta) & \frac{i \sin(2\theta)}{2} & -\sin^2(\theta) & 0 & 0 & 0 & 0 \\ -\sin^2(\theta) & \frac{i \sin(2\theta)}{2} & \cos^2(\theta) & \frac{i \sin(2\theta)}{2} & 0 & 0 & 0 & 0 \\ 0 & 0 & \frac{i \sin(2\theta)}{2} & \cos^2(\theta) & \frac{i \sin(2\theta)}{2} & -\sin^2(\theta) & 0 & 0 \\ 0 & 0 & -\sin^2(\theta) & \frac{i \sin(2\theta)}{2} & \cos^2(\theta) & \frac{i \sin(2\theta)}{2} & 0 & 0 \\ 0 & 0 & 0 & 0 & \frac{i \sin(2\theta)}{2} & \cos^2(\theta) & \frac{i \sin(2\theta)}{2} & -\sin^2(\theta) \\ 0 & 0 & 0 & 0 & -\sin^2(\theta) & \frac{i \sin(2\theta)}{2} & \cos^2(\theta) & \frac{i \sin(2\theta)}{2} \\ \frac{i \sin(2\theta)}{2} & -\sin^2(\theta) & 0 & 0 & 0 & 0 & \frac{i \sin(2\theta)}{2} & \cos^2(\theta) \end{bmatrix} \quad (2.12)$$

Matrix \mathbf{U} defines a cellular automaton. The pair of matrices \mathbf{U}_0 and \mathbf{U}_1 suggests a more fine-grained cellular evolution of the original Hamiltonian, by alternately applying \mathbf{U}_0 and \mathbf{U}_1 to the quantum state $\Psi(x)$. An even-numbered cell interacts alternately with its right-hand side and left-hand side neighbors. For odd-numbered cells the order of interaction is opposite. The cell-update rules of \mathbf{U} have a bounded neighborhood, including both immediate neighbors and one of the neighbors at distance two. Matrix \mathbf{U} has nonzero elements in the top-right and bottom-left corners, consistent with the periodic boundary conditions. Subsection 2.5 presents a bounded, non-periodic, SCA.

Cellular automaton $\mathbf{U}_1\mathbf{U}_0$ is a so-called *partitioning cellular automaton*, (a.k.a. block cellular automaton) pioneered by Margolus and Toffoli ([40], pp 119-120). The N cells are partitioned in two ways, each with a matching *block rule* (\mathbf{U}_0 and \mathbf{U}_1), applied alternately.

The $\mathcal{O}(\theta^2)$ term (2.10) is the so-called spectral-norm (approximation) error, which can be made arbitrarily small by choosing a small time step τ (a small θ). This approximation can be improved [37] by

$$\exp(-i\theta\hat{\mathbf{H}}) = \exp(-i\frac{\theta}{2}\hat{\mathbf{H}}_0) \exp(-i\theta\hat{\mathbf{H}}_1) \exp(-i\frac{\theta}{2}\hat{\mathbf{H}}_0) + \mathcal{O}(\theta^3). \quad (2.13)$$

The SCA experiments in later sections are based on the alternate application of $\mathbf{U}_1\mathbf{U}_0$ and $\mathbf{U}_0\mathbf{U}_1$, according to this improved approximation. Section 3 proposes alternative measures for the approximation error, in terms of (phase and group) velocities and energy levels.

²Matrix $\mathbf{C} = \exp(-i\theta)R_x(-2\theta)$, where $R_x(-2\theta)$ is the qubit rotation operator.

³Matrix \mathbf{U} has eigenvalue $\lambda=1$ with eigenvector $[1, 1, \dots, 1]^\top$; each row sum (column sum) equals 1.

2.3 A 3-dimensional SCA for a free particle

A 3D SCA operates on wave function Ψ represented by a 3D matrix of $N = N_X N_Y N_Z$ cells, with N_X, N_Y, N_Z even. This SCA can be represented by 2D matrix \mathbf{U}_{XYZ} , such that

$$\text{vec}(\Psi(t+\tau)) = \mathbf{U}_{XYZ} \text{vec}(\Psi(t)) , \quad (2.14)$$

where $\text{vec}(\mathbf{M})$ denotes the standard vectorization of matrix \mathbf{M} . (In two dimensions, $\text{vec}(\mathbf{M})$ is obtained by stacking the columns of the \mathbf{M} on top of one another.) First, matrix \mathbf{U}_{XYZ} is derived from the Hamiltonian of a free particle, expressed in terms of 1D SCAs of (2.10). In Subsection 2.4 an SCA for the complete Schrödinger Hamiltonian (1.1) will be derived.

A 2D version of discrete Hamiltonian (2.1) is given by

$$\begin{aligned} \mathbf{H}\Psi(x, t) = -\delta_m(& \Psi(x-1, y, t) - 2\Psi(x, y, t) + \Psi(x+1, y, t) \\ & \Psi(x, y-1, t) - 2\Psi(x, y, t) + \Psi(x, y+1, t)) . \end{aligned} \quad (2.15)$$

In matrix form, the Hamiltonian can be split as in \mathbf{H}_{XY} , where each of the two terms corresponds to a line of (2.15):

$$\begin{aligned} \mathbf{H}_{XY} &= \mathbf{I}_X \otimes \mathbf{H}_Y + \mathbf{K}_{XY}(\mathbf{I}_Y \otimes \mathbf{H}_X)\mathbf{K}_{XY}^\top \\ \mathbf{H}_X &= \mathbf{I}_{X2} \otimes \mathbf{B} + \mathbf{S}^{-1}(\mathbf{I}_{X2} \otimes \mathbf{B}) \mathbf{S} \\ \mathbf{H}_Y &= \mathbf{I}_{Y2} \otimes \mathbf{B} + \mathbf{S}^{-1}(\mathbf{I}_{Y2} \otimes \mathbf{B}) \mathbf{S} . \end{aligned} \quad (2.16)$$

Here identity matrix \mathbf{I}_X is of size N_X and \mathbf{I}_{X2} of size $N_X/2$. Matrix \mathbf{K}_{XY} is a shorthand for the so-called *commutation matrix* $\mathbf{K}^{(N_X, N_Y)}$ and is defined by $\mathbf{K}^{(m, n)} \text{vec}(\mathbf{M}) = \text{vec}(\mathbf{M}^\top)$ for $m \times n$ matrix \mathbf{M} . Note that with $\mathbf{K}_{YX} = (\mathbf{K}_{XY})^\top = (\mathbf{K}_{XY})^{-1}$. The two terms of \mathbf{H}_{XY} commute, that is,

$$[\mathbf{I}_X \otimes \mathbf{H}_Y, \mathbf{K}_{XY}(\mathbf{I}_Y \otimes \mathbf{H}_X)\mathbf{K}_{XY}^\top] = 0 . \quad (2.17)$$

Hence, since matrices \mathbf{K} are orthogonal,

$$\begin{aligned} \exp(-i\frac{\tau}{\hbar}\mathbf{H}_{XY}) &= \exp(-i\frac{\tau}{\hbar}(\mathbf{I}_X \otimes \mathbf{H}_Y)) \cdot \exp\left(-i\frac{\tau}{\hbar}(\mathbf{K}_{XY}(\mathbf{I}_Y \otimes \mathbf{H}_X)\mathbf{K}_{XY}^\top)\right) \\ &= (\mathbf{I}_X \otimes \exp(-i\frac{\tau}{\hbar}\mathbf{H}_Y)) \cdot (\mathbf{K}_{XY}(\mathbf{I}_Y \otimes \exp(-i\frac{\tau}{\hbar}\mathbf{H}_X)\mathbf{K}_{XY}^\top)) \\ &= (\mathbf{I}_X \otimes \mathbf{U}_Y) \cdot \mathbf{K}_{XY}(\mathbf{I}_Y \otimes \mathbf{U}_X) \mathbf{K}_{XY}^\top + \mathcal{O}(\theta^2) \\ &= \mathbf{U}_X \otimes \mathbf{U}_Y + \mathcal{O}(\theta^2) \end{aligned} \quad (2.18)$$

where 2D SCA $\mathbf{U}_{XY} = \mathbf{U}_X \otimes \mathbf{U}_Y$ is constructed from 1D SCA (2.10):

$$\begin{aligned} \mathbf{U}_X &= \mathbf{U}_{X,1} \mathbf{U}_{X,0} & \mathbf{U}_{X,0} &= \mathbf{I}_{X2} \otimes \mathbf{C} & \mathbf{U}_{X,1} &= \mathbf{S}^{-1}(\mathbf{I}_{X2} \otimes \mathbf{C}) \mathbf{S} \\ \mathbf{U}_Y &= \mathbf{U}_{Y,1} \mathbf{U}_{Y,0} & \mathbf{U}_{Y,0} &= \mathbf{I}_{Y2} \otimes \mathbf{C} & \mathbf{U}_{Y,1} &= \mathbf{S}^{-1}(\mathbf{I}_{Y2} \otimes \mathbf{C}) \mathbf{S} . \end{aligned} \quad (2.19)$$

Alternatively,

$$\mathbf{U}_{XY} = (\mathbf{U}_{X,1} \otimes \mathbf{U}_{Y,1}) \cdot (\mathbf{U}_{X,0} \otimes \mathbf{U}_{Y,0}) \quad (2.20)$$

which describes an SCA-evolution using the 2×2 blocks of the Margolus neighborhood [40].

For the 3D case, Hamiltonian \mathbf{H}_{XYZ} can be written as a sum of three mutually commuting terms, similar to (2.16). The resulting 3D SCA, using $\mathbf{K}_{XYZ} = \mathbf{K}^{(N_X, N_Y, N_Z)}$, is

$$\begin{aligned} & \mathbf{U}_{XYZ} \\ &= (\mathbf{U}_X \otimes \mathbf{U}_Y \otimes \mathbf{U}_Z) \\ &= (\mathbf{I}_X \otimes \mathbf{I}_Y \otimes \mathbf{U}_Z) \cdot (\mathbf{I}_X \otimes \mathbf{U}_Y \otimes \mathbf{I}_Z) \cdot (\mathbf{U}_X \otimes \mathbf{I}_Y \otimes \mathbf{I}_Z) \\ &= (\mathbf{I}_X \otimes \mathbf{I}_Y \otimes \mathbf{U}_Z) \cdot (\mathbf{I}_X \otimes \mathbf{K}_{YZ}(\mathbf{I}_Z \otimes \mathbf{U}_Y) \mathbf{K}_{YZ}^\top) \cdot (\mathbf{K}_{XYZ}(\mathbf{I}_Y \otimes \mathbf{I}_Z \otimes \mathbf{U}_X) \mathbf{K}_{XYZ}^\top) . \end{aligned} \quad (2.21)$$

2.4 A 3-dimensional SCA, incl. $\phi(\mathbf{x})$ and $\mathbf{A}(\mathbf{x})$

The complete Schrödinger Hamiltonian (1.1) can be rewritten according to

$$\begin{aligned}
& \left(\frac{1}{2m} \left(\frac{\hbar}{i} \nabla - q\mathbf{A}(\mathbf{x}) \right) \cdot \left(\frac{\hbar}{i} \nabla - q\mathbf{A}(\mathbf{x}) \right) + q\phi(\mathbf{x}) \right) \Psi \\
&= \left(-\frac{\hbar^2}{2m} \nabla^2 + \left(q\phi(\mathbf{x}) + \frac{q^2}{2m} |\mathbf{A}(\mathbf{x})|^2 \right) + i\frac{q\hbar}{2m} (\nabla \cdot \mathbf{A}(\mathbf{x}) + \mathbf{A}(\mathbf{x}) \cdot \nabla) \right) \Psi \\
&= -\frac{\hbar^2}{2m} \nabla^2 \Psi + \left(q\phi(\mathbf{x}) + \frac{q^2}{2m} |\mathbf{A}(\mathbf{x})|^2 \right) \Psi + i\frac{q\hbar}{2m} (\Psi \nabla \cdot \mathbf{A}(\mathbf{x}) + 2\mathbf{A}(\mathbf{x}) \cdot \nabla \Psi) \\
&= -\frac{\hbar^2}{2m} \nabla^2 \Psi + \left(q\phi(\mathbf{x}) + \frac{q^2}{2m} |\mathbf{A}(\mathbf{x})|^2 \right) \Psi + i\frac{q\hbar}{2m} (2\mathbf{A}(\mathbf{x}) \cdot \nabla \Psi) .
\end{aligned} \tag{2.22}$$

Here $\nabla \cdot \mathbf{A}(\mathbf{x})$ is chosen to equal 0 (the Coulomb gauge), without loss of generality. A discrete-space version of this Hamiltonian can be described by

$$\begin{aligned}
\Psi(t + \tau) = & D_X(\mathbf{x})\Psi(x-1, y, z, t) + 2C(\mathbf{x})\Psi(\mathbf{x}, t) + D_X^*(\mathbf{x})\Psi(x+1, y, z, t) \\
& + D_Y(\mathbf{x})\Psi(x, y-1, z, t) + 2C(\mathbf{x})\Psi(\mathbf{x}, t) + D_Y^*(\mathbf{x})\Psi(x, y+1, z, t) \\
& + D_Z(\mathbf{x})\Psi(x, y, z-1, t) + 2C(\mathbf{x})\Psi(\mathbf{x}, t) + D_Z^*(\mathbf{x})\Psi(x, y, z+1, t) ,
\end{aligned} \tag{2.23}$$

with, for $W \in \{X, Y, Z\}$

$$\begin{aligned}
C(\mathbf{x}) &= \delta_m + \frac{1}{3} \frac{1}{2} \left(q\phi(\mathbf{x}) + \frac{\delta_q^2}{\delta_m} |\mathbf{A}(\mathbf{x})|^2 \right) \\
D_W(\mathbf{x}) &= -\delta_m - 2i\delta_q A_W(\mathbf{x}) ,
\end{aligned} \tag{2.24}$$

where δ_m (as before) and δ_q are given by

$$\delta_m = \frac{1}{2m} \frac{\hbar^2}{a^2} , \quad \delta_q = \frac{q}{2m} \frac{\hbar}{a} , \quad \frac{\delta_q^2}{\delta_m} = \frac{q^2}{2m} . \tag{2.25}$$

The factors $\frac{1}{3}$ and $\frac{1}{2}$ correspond to the 3D split and the even/odd splits of the Hamiltonian. In matrix form, it can be expressed in terms of 1D split Hamiltonians, such as

$$\begin{aligned}
\mathbf{H}_X(\mathbf{x}) &= \bigoplus_{x=0}^{N_X/2} \mathbf{B}_X(2x, y, z) + \mathbf{S}^{-1} \left(\bigoplus_{x=0}^{N_X/2} \mathbf{B}_X(2x+1 \bmod N_X, y, z) \right) \mathbf{S} \\
\mathbf{B}_W(\mathbf{x}) &= \begin{bmatrix} C(\mathbf{x}) & D_W(\mathbf{x}) \\ D_W^*(\mathbf{x}) & C(\mathbf{x}) \end{bmatrix} ,
\end{aligned} \tag{2.26}$$

where \oplus denotes the *direct matrix sum*, not to be confused with the Kronecker sum. The expressions for $\mathbf{H}_Y(\mathbf{x})$ and $\mathbf{H}_Z(\mathbf{x})$ are similar. For 3D Hamiltonian \mathbf{H}_{XYZ} each of the three terms corresponds to a line of (2.23):

$$\begin{aligned}
\mathbf{H}_{XYZ} = & \left(\bigoplus_{x=0}^{N_X-1} \bigoplus_{y=0}^{N_Y-1} \mathbf{H}_Z(\mathbf{x}) \right) \\
& + \left(\bigoplus_{x=0}^{N_X-1} \mathbf{K}_{YZ} \left(\bigoplus_{z=0}^{N_Z-1} \mathbf{H}_Y(\mathbf{x}) \right) \mathbf{K}_{YZ}^\top \right) \\
& + \left(\mathbf{K}_{XYZ} \left(\bigoplus_{y=0}^{N_Y-1} \bigoplus_{z=0}^{N_Z-1} \mathbf{H}_X(\mathbf{x}) \right) \mathbf{K}_{XYZ}^\top \right) .
\end{aligned} \tag{2.27}$$

Unlike Hamiltonian (2.16) the matrix terms of (2.27) do *not* commute with one another. Three-dimensional Schrödinger cellular automaton \mathbf{U}_{XYZ} is given by

$$\begin{aligned}
\exp(-i\frac{\tau}{\hbar} \mathbf{H}_{XYZ}) &= \mathbf{U}_{XYZ} + \mathcal{O}(\tau^2) \\
\mathbf{U}_{XYZ} &= \left(\bigoplus_{x=0}^{N_X-1} \bigoplus_{y=0}^{N_Y-1} \mathbf{U}_{Z1}(\mathbf{x}) \mathbf{U}_{Z0}(\mathbf{x}) \right) \\
& \quad \left(\bigoplus_{x=0}^{N_X-1} \mathbf{K}_{YZ} \left(\bigoplus_{z=0}^{N_Z-1} \mathbf{U}_{Y1}(\mathbf{x}) \mathbf{U}_{Y0}(\mathbf{x}) \right) \mathbf{K}_{YZ}^\top \right) \\
& \quad \left(\mathbf{K}_{XYZ} \left(\bigoplus_{y=0}^{N_Y-1} \bigoplus_{z=0}^{N_Z-1} \mathbf{U}_{X1}(\mathbf{x}) \mathbf{U}_{X0}(\mathbf{x}) \right) \mathbf{K}_{XYZ}^\top \right) ,
\end{aligned} \tag{2.28}$$

where $\mathbf{U}_{X0}(\mathbf{x})$ and $\mathbf{U}_{X1}(\mathbf{x})$ are defined by

$$\begin{aligned}\exp(-i\frac{\tau}{h}\mathbf{H}_X(\mathbf{x})) &= \mathbf{U}_{X1}(\mathbf{x}) \cdot \mathbf{U}_{X0}(\mathbf{x}) + \mathcal{O}(\tau^2) \\ \mathbf{U}_{X0}(\mathbf{x}) &= \bigoplus_{x=0}^{N_X/2} \mathbf{C}_X(2x, y, z) \\ \mathbf{U}_{X1}(\mathbf{x}) &= \mathbf{S}^{-1} \left(\bigoplus_{x=0}^{N_X/2} \mathbf{C}_X(2x+1 \bmod N_X, y, z) \right) \mathbf{S} \\ \mathbf{C}_W(\mathbf{x}) &= \exp[(-i\frac{\tau}{h} \mathbf{B}_W(\mathbf{x}))],\end{aligned}\tag{2.29}$$

and likewise for \mathbf{U}_{Y0} , \mathbf{U}_{Y1} , \mathbf{U}_{Z0} , and \mathbf{U}_{Z1} . As with (2.13), the approximation error can be reduced to $\mathcal{O}(\tau^3)$ by suitably alternating the evolution order of the six U_{W_i} involved.

2.5 Reflective cells $X(\mathbf{x})$

How can a position-dependent potential-energy function $V(\mathbf{x}) = q\phi(\mathbf{x})$ be used to introduce boundary conditions for $\Psi(\mathbf{x})$? In a one-dimensional SCA, $V(x)$ can be included in the Hamiltonian matrix as in

$$\hat{\mathbf{H}}' = \hat{\mathbf{H}} + \hat{\mathbf{V}} \quad \hat{\mathbf{V}} = \text{diag} \left(\frac{1}{\delta_m} V(x, y) \right), \tag{2.30}$$

corresponding to the evolution matrix

$$\begin{aligned}\mathbf{U}' = \exp(-i\theta(\hat{\mathbf{H}} + \hat{\mathbf{V}})) &= \exp(-i\theta\hat{\mathbf{H}}) \exp(-i\theta\hat{\mathbf{V}}) + \mathcal{O}(\theta^2) \\ &= \exp(-i\theta\hat{\mathbf{H}}) \exp(-i\theta(\hat{\mathbf{V}} + 2\frac{n}{\theta}\pi)) + \mathcal{O}(\theta^2).\end{aligned}\tag{2.31}$$

Note that \mathbf{U}' is periodic in the potential, which limits the use of $V(x)$. In particular, it can be shown that no real-valued $V(x)$ can cancel the off-diagonal nonzeros of matrix $\mathbf{U}_1\mathbf{U}_0$ in (2.12). Hence, $V(x)$ cannot be used to remove the periodic boundaries.

For a bounded SCA, one with reflective (non-periodic) boundaries, matrix $\mathbf{U}_0 = \mathbf{I}_M \otimes \mathbf{C}$ in (2.10) can be replaced by one where for the last block rotation angle $\theta = \pi$, as in

$$\mathbf{U}_{b1} = \mathbf{S}^{-1} \text{diag}(\mathbf{C}, \mathbf{C}, \dots, \mathbf{C}, \exp(-i\pi\mathbf{B})) \mathbf{S}. \tag{2.32}$$

For $N=8$

$$\mathbf{U}_{b1} = \exp(-i\theta) \times \begin{bmatrix} -e^{i\theta} & 0 & 0 & 0 & 0 & 0 & 0 & 0 \\ 0 & \cos(\theta) & i \sin(\theta) & 0 & 0 & 0 & 0 & 0 \\ 0 & i \sin(\theta) & \cos(\theta) & 0 & 0 & 0 & 0 & 0 \\ 0 & 0 & 0 & \cos(\theta) & i \sin(\theta) & 0 & 0 & 0 \\ 0 & 0 & 0 & i \sin(\theta) & \cos(\theta) & 0 & 0 & 0 \\ 0 & 0 & 0 & 0 & 0 & \cos(\theta) & i \sin(\theta) & 0 \\ 0 & 0 & 0 & 0 & 0 & i \sin(\theta) & \cos(\theta) & 0 \\ 0 & 0 & 0 & 0 & 0 & 0 & 0 & -e^{i\theta} \end{bmatrix}. \tag{2.33}$$

Crucially, $\mathbf{U}_{b1}[0, 7] = \mathbf{U}_{b1}[7, 0] = 0$, unlike in (2.11). Matrix \mathbf{U}_{b1} is *not* circulant, and the corresponding cellular automaton $\mathbf{U}_{b1}\mathbf{U}_{b0}$ has no periodic boundaries, but a reflective (two-sided) boundary at position $N-1$. Such *reflective cells* can be placed at any position \mathbf{x} , and can thus be used to model, for example, an infinite potential well (Subsection 3.4), or a double-slitted screen (Subsection 4.4).

2.6 A Schrödinger quantum walk

A one-dimensional Schrödinger QW for a free particle, comprising $2M$ cells, and with periodic boundary conditions is presented next. State vector $|\Psi\rangle$ can be split into even and odd cells, as in

$$|\Psi\rangle = \sum_{n=0}^{M-1} (\gamma_{2n} |2n\rangle + \gamma_{2n+1} |2n+1\rangle) , \quad (2.34)$$

where γ_i is a complex number. This state can be “curled up” as in [3]

$$|\tilde{\Psi}\rangle = \sum_{n=0}^{M-1} (\alpha_n |\uparrow\rangle + \beta_n |\downarrow\rangle) \otimes |n\rangle , \quad \alpha_n = \gamma_{2n} \text{ and } \beta_n = \gamma_{2n+1} , \quad (2.35)$$

where two adjacent cells are combined into a single, non-normalized, qubit. A corresponding two-step QW evolution operator can be described by matrix $\tilde{\mathbf{U}}$

$$\tilde{\Psi}(t+1) = \tilde{\mathbf{U}} \tilde{\Psi}(t) , \quad \tilde{\mathbf{U}} = \tilde{\mathbf{S}}^{-1}(\mathbf{C} \otimes \mathbf{I}_M) \tilde{\mathbf{S}} (\mathbf{C} \otimes \mathbf{I}_M) . \quad (2.36)$$

Here \mathbf{C} is the so-called coin, which for the Schrödinger QW is given by (2.10). QW-shifts $\tilde{\mathbf{S}}$ and its inverse are given by

$$\begin{aligned} \tilde{\mathbf{S}} &= \sum_{n=0}^{M-1} (|\downarrow\rangle\langle\uparrow| \otimes |(n-1)_M\rangle\langle n_M| + |\uparrow\rangle\langle\downarrow| \otimes |n_M\rangle\langle n_M|) \\ \tilde{\mathbf{S}}^{-1} &= \sum_{n=0}^{M-1} (|\downarrow\rangle\langle\uparrow| \otimes |n_M\rangle\langle n_M| + |\uparrow\rangle\langle\downarrow| \otimes |(n+1)_M\rangle\langle n_M|) , \end{aligned} \quad (2.37)$$

where n_M is a shorthand for $n \bmod M$. Shift operator $\tilde{\mathbf{S}}$ keeps the down-part of the state at its position and moves the up-part to the left. The inverse operator $\tilde{\mathbf{S}}^{-1}$ does the opposite.

The QW in the form (2.36) can be found as staggered QW in [36] and as alternating QW in [12]. As shown Costa et al [14], staggered QWs are a subset of PUQCs. Indeed, the QW above is structurally very similar to the evolution operator $\mathbf{U}_1 \mathbf{U}_0$ of (2.10),

$$\mathbf{U} = \mathbf{U}_1 \mathbf{U}_0 = \mathbf{S}^{-1}(\mathbf{I}_M \otimes \mathbf{C}) \mathbf{S} (\mathbf{I}_M \otimes \mathbf{C}) . \quad (2.38)$$

QWs typically use different coins \mathbf{C} , including Hadamard, Fourier, and Grover coins. Alternatively, the SCA based on these coins also specify unitary cellular automata.

The SCA and the staggered QW are like two sides of the same medal. A CA appears to be more natural as a solution of the Schrödinger equation, while a QW is a more natural way to model search. It is comparable with the classical Markov processes, and the backward and forward Kolmogorov equations: the forward equations, also called Fokker-Planck equations, are used to describe the evolution of the probability distribution, which is perfectly suited for a CA, while the backward equations are used to compute the probability to reach a certain state.

3 Experiments with 1D Schrödinger cellular automata

In this section the results of the evolution of 1D SCA are compared with known analytical solutions for various textbook Hamiltonians.

3.1 A plane wave in a periodic SCA

In a first experiment a 1D SCA is initialized with a plane wave. Cell x has position xa for integer cell index x and cell size a . A plane wave at time $t=0$ as a function of x , with spatial offset x_0 and wavenumber k , can be described by W_{plane}

$$W_{plane}(x, x_0, k) = e^{ik(x-x_0)} . \quad (3.1)$$

Note that also wavenumber k is scaled by cell size a such that $k = a2\pi/\lambda$, and as a result is dimensionless. An initial state of a cellular automata can be obtained by sampling W_{plane} at each individual cell index. A given cell size a implies a shortest possible wavelength, viz. $\lambda=2a$, which corresponds to $k=\pi$. Sampling of W_{plane} at discrete positions leads to a form of spatial aliasing, since, for integer n

$$W_{plane}(x, x_0, k + 2n\pi) = W_{plane}(x, x_0, k) . \quad (3.2)$$

This aliasing has important implications for phase velocity, dispersion, group velocity, and energy levels, as is explored below.

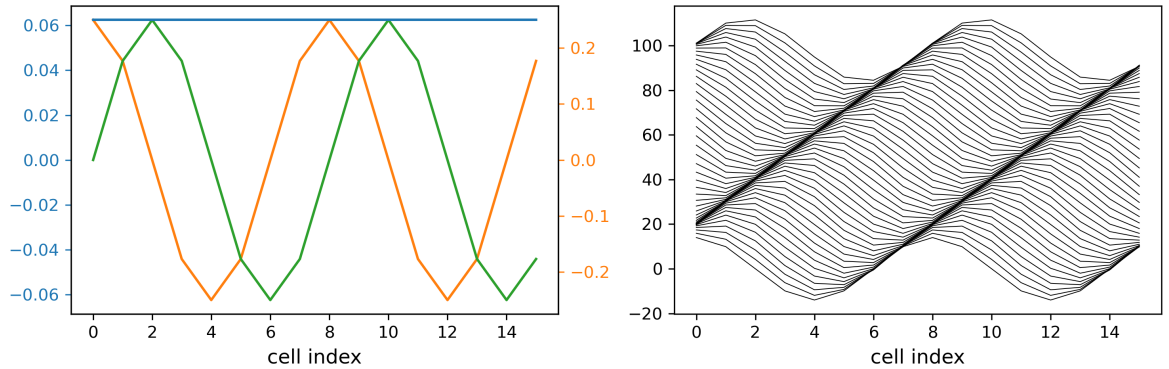


Figure 1: (left) $\Psi(x, t=0)$ is plane wave with $\text{Re}(\Psi)$ in orange, $\text{Im}(\Psi)$ in green, and $|\Psi|^2$ in blue; (right) the plane wave moves rightwards over 100 iterations, two at a time.

The first cellular automaton comprises 16 cells with $\theta = \frac{\pi}{24}$. It is initialized with W_{plane} with k chosen such that precisely two wavelengths fit in the 16 cells. Figure 1 shows this initial state and its evolution over 100 cycles. The integrated probability $P(t)$ remains very close to 1. After as many as 100k cycles $|P-1| \approx 10^{-11}$, without any form of normalization. The plane wave moves rightwards with a phase velocity of about 10 cells per 100 cycles, $\approx 0.1 [a/\tau]$. Below the phase velocity is calculated as *half* the displacement of a plane wave over *two* evolution steps, based on the alternate application of $\mathbf{U}_1\mathbf{U}_0$ and $\mathbf{U}_0\mathbf{U}_1$. The application

of two evolution steps to $\Psi(x, t_0) = e^{ikx}$ results in

$$\begin{aligned}
\Psi(x, t_0+1) &= (\mathbf{U}_1 \mathbf{U}_0) \cdot \Psi(x, t_0) \\
&= e^{ikx} e^{-2i\theta} \left(-\sin^2(\theta) e^{-2ik} + \frac{1}{2} i \sin(2\theta) e^{-ik} + \cos^2(\theta) + \frac{1}{2} i \sin(2\theta) e^{ik} \right) \\
&= e^{ik(x-v_{10})} , \\
\text{where } v_{10} &= \frac{1}{k} \left(2\theta - \ln \left(\cos^2(\theta) - \sin^2(\theta) e^{-2ik} + i \sin(2\theta) \cos(k) \right) \right) . \\
\Psi(x, t_0+2) &= (\mathbf{U}_0 \mathbf{U}_1) \cdot \Psi(x, t_0+1) = (\mathbf{U}_0 \mathbf{U}_1) \cdot e^{ik(x-v_{10})} \\
&= e^{ik(x-v_{10})} e^{-2i\theta} \left(-\sin^2(\theta) e^{2ik} + \frac{1}{2} i \sin(2\theta) e^{-ik} + \cos^2(\theta) + \frac{1}{2} i \sin(2\theta) e^{ik} \right) \\
&= e^{ik(x-(v_{10}+v_{01}))} , \\
\text{where } v_{01} &= \frac{1}{k} \left(2\theta - \ln \left(\cos^2(\theta) - \sin^2(\theta) e^{2ik} + i \sin(2\theta) \cos(k) \right) \right) .
\end{aligned} \tag{3.3}$$

The Taylor expansion of both \ln functions, assisted by Python/Sympy, results in

$$\begin{aligned}
v_{10} &= \frac{4\theta}{k} \sin^2 \left(\frac{k}{2} \right) + \frac{\theta^2}{k} \sin(k) + \frac{4\theta^3}{3k} \left(\cos(k) \sin^2(k) - 3i \sin(k) \cos^2(k) \right) \\
&\quad - \frac{\theta^4}{6k} (8 \sin(2k) + 3 \sin(4k)) + \mathcal{O}(\theta^5) \\
v_{01} &= \frac{4\theta}{k} \sin^2 \left(\frac{k}{2} \right) - \frac{\theta^2}{k} \sin(k) + \frac{4\theta^3}{3k} \left(\cos(k) \sin^2(k) + 3i \sin(k) \cos^2(k) \right) \\
&\quad + \frac{\theta^4}{6k} (8 \sin(2k) + 3 \sin(4k)) + \mathcal{O}(\theta^5) .
\end{aligned} \tag{3.4}$$

Note that both v_{10} and v_{01} are complex and that the imaginary terms as well as the (real) θ^2 and θ^4 terms in v_{10} and v_{01} have opposite signs. Finally, phase velocity $v_p(\theta, k)$ is given by

$$\begin{aligned}
v_p(\theta, k) &= \frac{1}{2} (v_{10} + v_{01}) \\
&= \frac{4\theta}{k} \sin^2 \left(\frac{k}{2} \right) + \frac{4\theta^3}{3k} \cos(k) \sin^2(k) + \mathcal{O}(\theta^5) ,
\end{aligned} \tag{3.5}$$

where the imaginary, θ^2 , and θ^4 contributions cancel each other. This cancelation is a direct consequence of the alternating application of $\mathbf{U}_1 \mathbf{U}_0$ and $\mathbf{U}_0 \mathbf{U}_1$ and is consistent with the spectral-norm approximation error in (2.13). For the experiment of Figure 1 this results in $v_p(\frac{\pi}{24}, \frac{\pi}{4}) = 0.098$, in agreement with the observed phase velocity.

The Lie-Trotter product formula applied to (2.10) gives

$$\exp(-i\theta(\hat{\mathbf{H}}_1 + \hat{\mathbf{H}}_0)) = \lim_{n \rightarrow \infty} \left(\exp\left(-i\frac{\theta}{n}\hat{\mathbf{H}}_1\right) \exp\left(-i\frac{\theta}{n}\hat{\mathbf{H}}_0\right) \right)^n . \tag{3.6}$$

The approximation error in $v_p(\theta, k)$ can be reduced by considering n smaller displacements over time τ/n . This suggests the following definition of the *base* phase velocity $\mathbf{v}_p(\theta, k)$.

$$\mathbf{v}_p(\theta, k) = \lim_{n \rightarrow \infty} n v_p\left(\frac{\theta}{n}, k\right) = \frac{4\theta}{k} \sin^2 \left(\frac{k}{2} \right) . \tag{3.7}$$

This base phase velocity corresponds to the phase velocity of the cellular automaton in the limit $\tau \rightarrow 0$. Hence, the $\mathcal{O}(\theta^3)$ term in (3.5) is the absolute error in phase velocity v_p as

introduced by splitting the Hamiltonian according to (2.13).⁴ The *relative* error in phase velocity v_p then becomes

$$\frac{v_p(\theta, k) - \mathbf{v}_p(\theta, k)}{\mathbf{v}_p(\theta, k)} = \theta^2 \frac{4 \cos(k) \sin^2(k)}{3 \sin^2\left(\frac{k}{2}\right)} + \mathcal{O}(\theta^4). \quad (3.8)$$

Figure 2 depicts the phase and base velocities versus k , as well as this relative error.

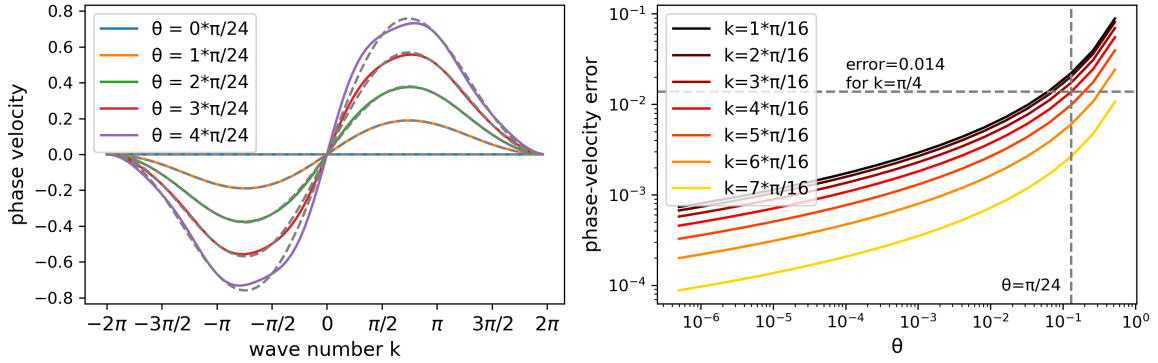


Figure 2: (left) Phase velocity v_p versus wave number k , $k \in [-2\pi, 2\pi]$, in units of $\frac{a}{\tau}$ for various θ . The coloured curves show the actual phase velocity $v_p(\theta, k)$ according to (3.5). The gray dashed curves show the base phase velocity $\mathbf{v}_p(\theta, k)$ according to (3.7). (right) The relative error in phase velocity versus θ according to (3.8).

3.2 A Gaussian wave packet in a periodic SCA

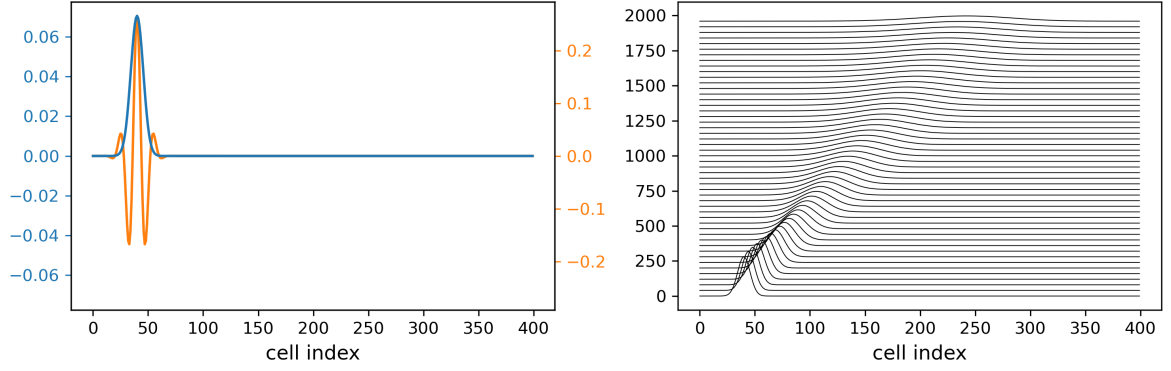
In the next experiment the same cellular automaton is initialized with a Gaussian wave packet of the form W_{packet} , using a normalization constant A .

$$W_{packet}(x, x_0, \sigma, k) = A \exp\left(-\frac{1}{2}\left(\frac{x - x_0}{\sigma}\right)^2\right) \exp(ik(x - x_0)). \quad (3.9)$$

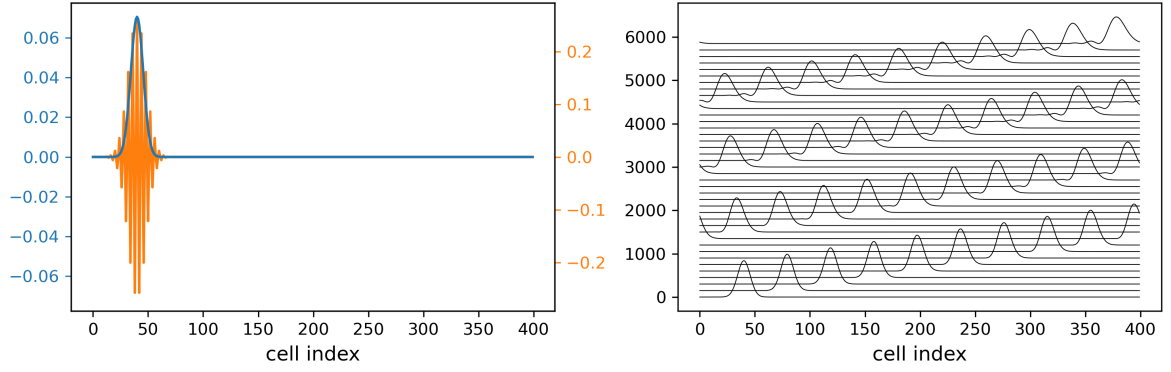
Figure 3a shows a wave packet W_{packet} , centered around position $x_0 = 40$ with $\sigma = 8$ and $k = \frac{\pi}{8}$. Note that the spatial extent of the wave packet appears to be less than three wavelengths. The wave packet moves rightwards rather slowly, fewer than 200 cells in 2000 cycles. Furthermore, it rapidly disperses. Figure 3b shows the same automaton initialized with a different wave packet with $\sigma = 8$ and $k = \frac{\pi}{2}$. Roughly ten wavelengths fit in the Gaussian envelope. It takes about 1600 cycles for a packet to traverse the width of the cellular automaton, and to reappear at the left hand side. The measured group velocity is ≈ 0.26 cells per cycle. After 8000 cycles the dispersion of the wave packet is visible as a minor pulse trailing the main wave packet.

A wave packet is composed of component sinusoidal waves of different wave numbers, each propagating with its own wavenumber-dependent phase velocity. The wave packet in Figure 3a has a center $k = \frac{\pi}{8}$. Component waves with a lower k move slower and those with a higher k faster. The dispersion of the second wave packet is substantially less, because of the smaller

⁴The relation between this error measure and the eigenvalue error [34] is a topic for further study.



(a) Wavenumber $k = \pi/8$: the wave packet is “sparse” and quickly disperses.



(b) Wavenumber $k = \pi/2$: the wave packet is “dense” and disperses much slower.

Figure 3: A Gaussian wave packet moves rightwards in a periodic SCA of 400 cells.

bandwidth $\Delta k/k$ of the wave packet. The component wave of the center frequency ($k = \frac{\pi}{2}$) moves fastest; all the other component waves move slower. (Recall that with $k = \frac{\pi}{2}$ the phase velocity of the center frequency of the wave packet is zero.)

It is common to derive the phase velocity from the so-called *dispersion relation* $\omega(k)$. Conversely, from (3.5) it follows that

$$\omega(\theta, k) = kv_p(\theta, k) = 4\theta \sin^2\left(\frac{k}{2}\right) + \frac{4}{3}\theta^3 \cos(k) \sin^2(k) + \mathcal{O}(\theta^5) . \quad (3.10)$$

The phase velocity v_p and group velocity v_g are related by

$$v_p = \frac{\omega}{k} \quad \text{and} \quad v_g = \frac{d\omega}{dk} . \quad (3.11)$$

Then from (3.5) it follows that

$$v_g(\theta, k) = \frac{d(kv_p)}{dk} = 2\theta \sin(k) + \frac{4}{3}\theta^3 \left(2 \sin(k) - 3 \sin^2(k)\right) + \mathcal{O}(\theta^5) . \quad (3.12)$$

As with the phase velocity, the $\mathcal{O}(\theta^3)$ contribution is the (absolute) approximation error.

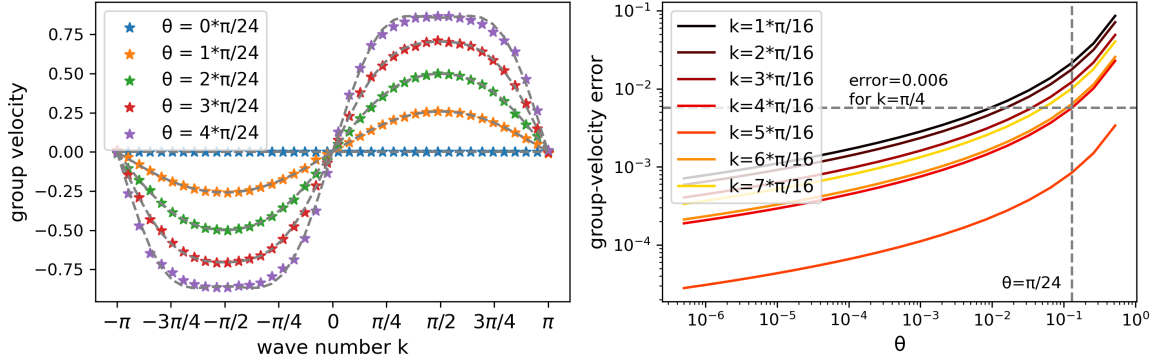


Figure 4: (left) Group velocity v_g versus wave number k for various θ in units of $\frac{\pi}{\tau}$. The colored \star markers denote *measured* group velocities from SCA evolutions. The dashed gray lines are based on (3.12). (right) The relative error in group velocity versus θ .

Figure 4 shows the measured group velocity v_g versus (θ, k) . These measurements are based on the displacement of the peak of the Gaussian envelope of the wave packet during a time interval of 200 cycles. The group velocity is periodic in k , approximately sinusoidal. It is well known that imposing periodic boundary conditions in space leads to discrete momenta. It is less well known is that discretization of space leads to periodic momenta. The momentum interval $[-\pi, \pi)$, used to depict $v_g(k)$, is known as the Brillouin zone.

3.3 A Gaussian wave packet in a bounded SCA

The cellular automaton of Figure 5a has reflective boundaries, as in (2.32). The initial wave packet has the same parameters as before: $\sigma = 8$ and $k = \frac{\pi}{2}$. During an evolution of 4000 cycles, the wave packet reflects twice at the boundary of the cellular automaton. With each bounce the wave packet interferes with itself and subsequently recovers.

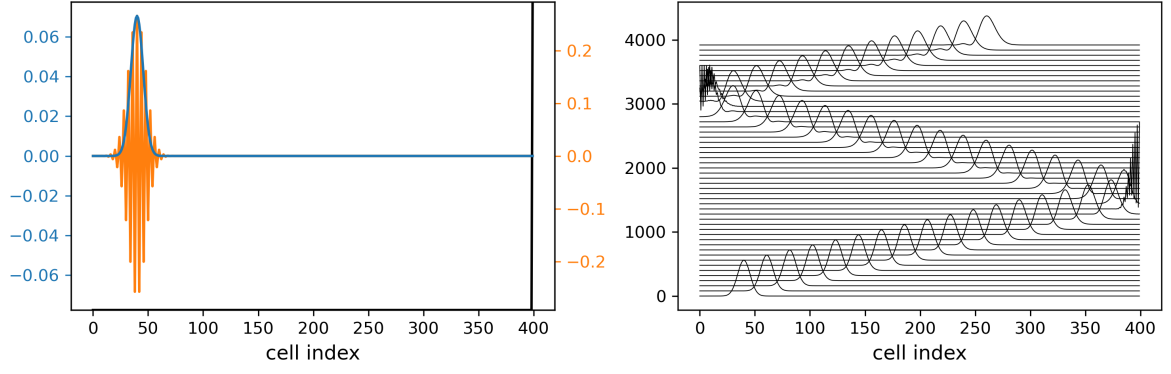
In addition to reflective boundaries, the cellular automaton of Figure 5b also has a narrow region in the middle with a potential $V(x) = 0.24\delta_m$, as indicated by the light gray line. The automaton is initialized with a wide wave packet and evolves for 2000 cycles. When the wave packet hits the high- $V(x)$ region, a smaller part is reflected and the main part proceeds into this region with a reduced group velocity and width. When this main part hits the backside of the high- $V(x)$ region, again a smaller part is reflected.

3.4 An infinite potential well:

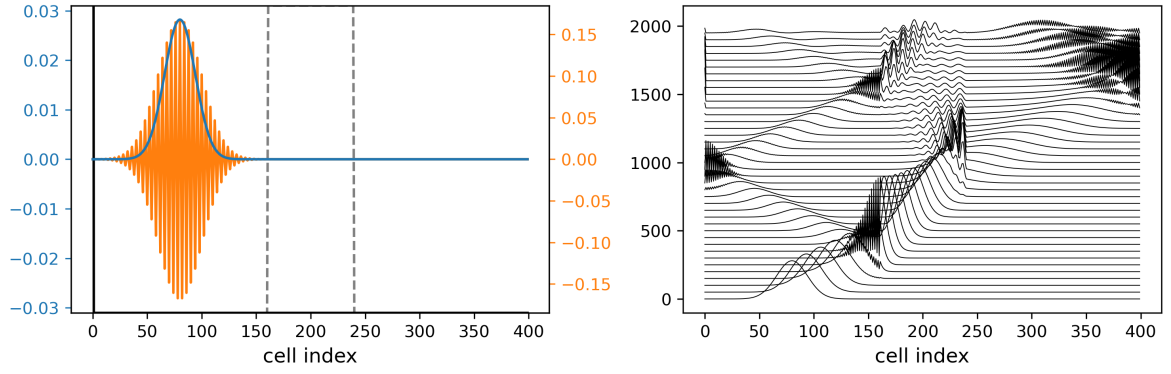
The next cellular automaton models an *infinite square well*, also known as a *particle in a box* (see e.g. [24]). The box has length $L = 17$ and is centered around $x_c = L/2$. Inside the box, $x_c - \frac{L}{2} < x < x_c + \frac{L}{2}$, the physical potential equals 0, outside the box it is infinite, and $\Psi_n(x, t) = 0$. The SCA comprises $L + 1$ cells, with a reflective cell (2.32) at $x = L$ to model the infinite potential. The initial state is, for integer $n \geq 0$,

$$W_{box}(x, x_c, L, n) = \sqrt{\frac{2}{L}} \sin\left(\frac{n\pi}{L}(x - x_c + L/2)\right). \quad (3.13)$$

W_{box} is subject to spatial aliasing: $W_{box}(x, x_c, L, n) = W_{box}(x, x_c, L, 2L+n)$, similar to W_{plane} (see Subsection 3.1). Interestingly, there is another, somewhat more subtle, symmetry. Let



(a) The wave packet is reflected on both sides.



(b) A region with a potential ($V = 0.12\delta_m$) causes refraction.

Figure 5: A wave packet in a cellular automaton of 400 cells with reflective boundaries.

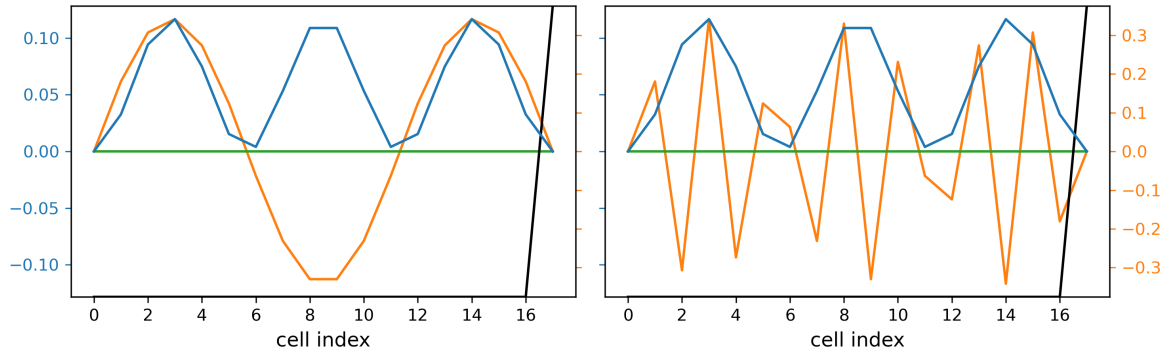


Figure 6: A cellular automaton with an infinite potential well with $L = 17$. (left) The initial state is $W_{box}(\dots, 3)$. (right) The initial state is $W_{box}(\dots, L-3)$.

$\Psi_n(t=0) = W_{box}(x, x_c, L, n)$ and $\Psi_{L-n}(t=0) = W_{box}(x, x_c, L, L-n)$. For $t \geq 0$, the corresponding $P(x, t)$ evolve in the same way, that is, $|\Psi_n(x, t)|^2 = |\Psi_{L-n}(x, t)|^2$. This symmetry is illustrated in Figure 6 for $L=17$ and $n=3$.

Figure 7 shows the evolution of the automaton for $n=3$. This evolution is periodic over time with a period of about 160 cycles. The analytic solution for $\Psi_n(x, t)$ for continuous space

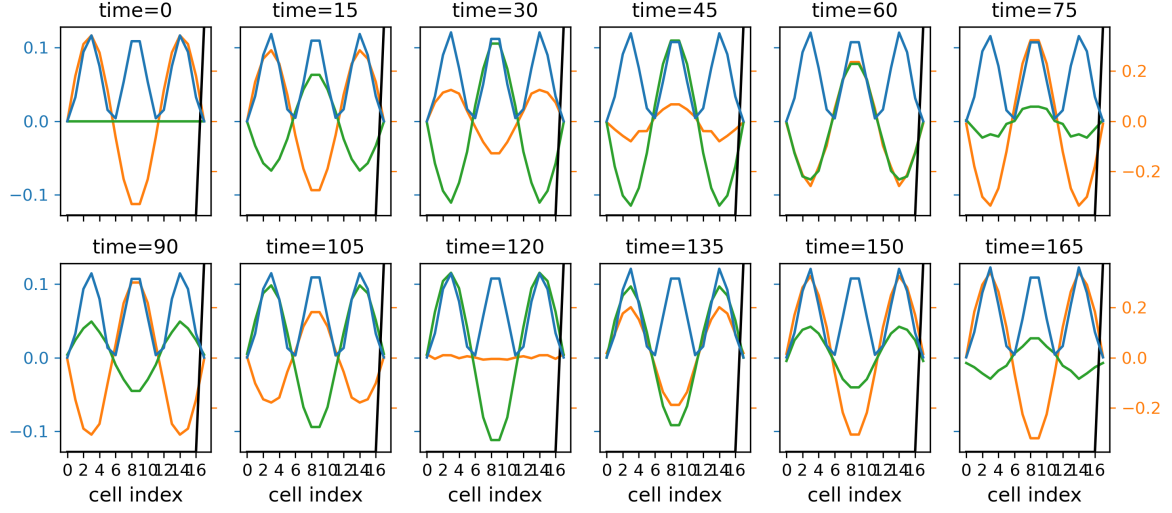


Figure 7: The evolution of the infinite-square-well automaton with $L = 17$. The colors orange, green, and blue denote $\text{Re}(\Psi_3(x, t))$, $\text{Im}(\Psi_3(x, t))$, and $P(\Psi_3(x, t))$ respectively.

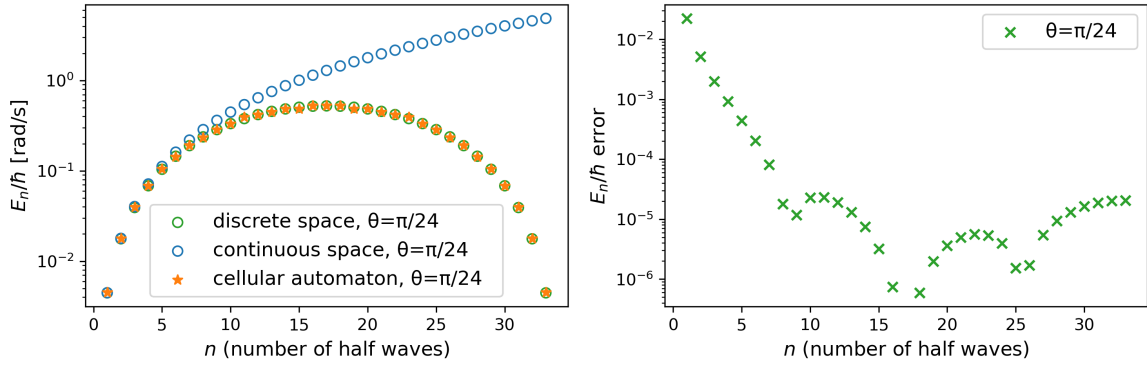


Figure 8: (left) The energy levels E_n/\hbar (in units of rad/s) versus n for an infinite square well. (right) The relative error in energy levels versus n .

is well known, see e.g. [24],

$$\Psi_n(x, t) = \sqrt{\frac{2}{L}} \sin\left(k_n\left(x - x_c + \frac{L}{2}\right)\right) e^{-i\omega_n t}, \quad (3.14)$$

where $k_n = \frac{n\pi}{L}$. The corresponding energy levels are

$$\frac{E_n}{\hbar} = \omega_n = \frac{n^2 \pi^2 \hbar}{2mL^2} = n^2 \pi^2 \left(\frac{a}{L}\right)^2 \frac{\theta}{\tau}. \quad (3.15)$$

Figure 8 (left) shows the matching energy levels, based dispersion relation (3.10). The orange stars are derived from the measured oscillation periods during the evolution of the cellular automaton initialized with $W_{box}(\dots, n)$. The green circles are based on the dispersion relation. The blue circles represent (3.15). Figure 8 (right) shows the relative error in energy levels versus n , which is defined analogously to (3.7) and (3.8). Energy E_n is symmetric in $n = L$ and periodic with period $2L$, as an immediate consequence of the earlier noted spatial aliasing resulting from the sampling of W_{box} .

3.5 A harmonic oscillator

The harmonic oscillator is based on a potential energy function that is parabolic in x

$$V(\underline{x}) = \frac{1}{2}\kappa\omega^2\underline{x}^2 = \frac{1}{2}m\omega^2\underline{x}^2, \quad (3.16)$$

where κ is the force constant. Coordinate \underline{x} is underlined to distinguish it from cell index x . The normalized stationary states for the harmonic oscillator are (e.g. [24]):

$$\psi_n(\underline{x}) = \left(\frac{m\omega}{\pi\hbar}\right)^{1/4} \frac{1}{\sqrt{2^n n!}} H_n(\xi) \exp(-\xi^2/2) \quad \text{with} \quad \xi = \sqrt{\frac{m\omega}{\hbar}} \underline{x}, \quad (3.17)$$

where n is the state number, ξ is a dimensionless variable, and $H_n(\xi)$ is the n th-order Hermite polynomial. For the experiment, state $n = 3$ is chosen. In order for the x -extent of the waveform to cover a significant portion of the $N = 400$ cells, x is scaled according to $x = \rho\xi$. The initial state then becomes

$$W_{\text{harmonic}}(x, n) = \psi_n(\rho\xi), \quad (3.18)$$

with $n = 3$ and $\rho = N/12$ for the experiment. The potential $V(x) = \frac{1}{2}\kappa(x - x_c)^2$ requires a value for κ . This value is obtained by iteratively tuning κ towards a stationary state for $n = 3$, with $\kappa = 2.18 \cdot 10^{-7} \delta_m$ as outcome.

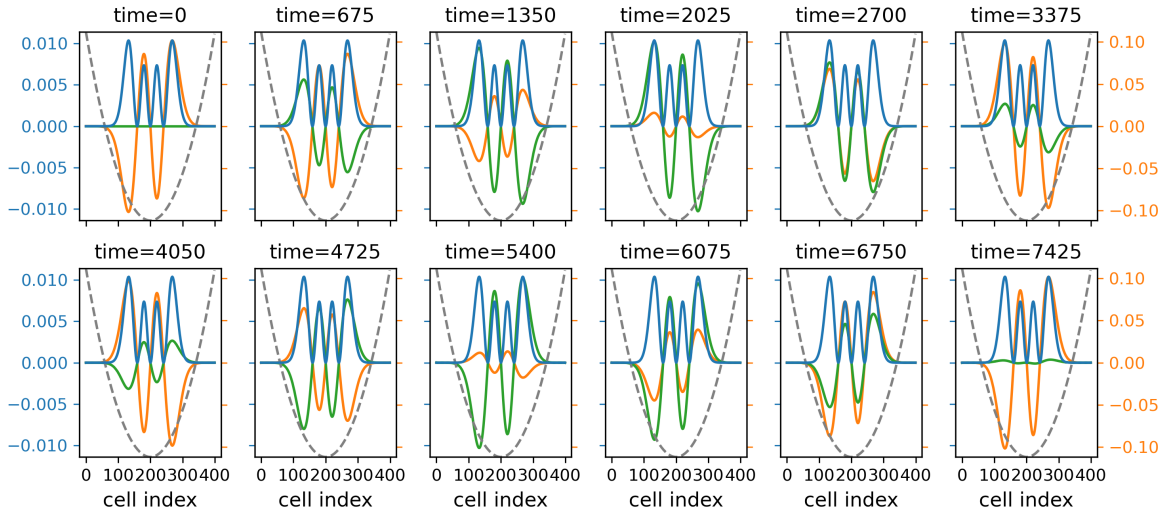


Figure 9: The evolution of a harmonic-oscillator CA initialized with $W_{\text{harmonic}}(x, 3)$. The dashed parabola represent $V(x)$. The measured oscillation period is 7425 cycles.

Figure 9 shows the evolution of the cellular automaton, where state $\Psi(x, t)$ is captured every 675 cycles. A single oscillation period lasts about 7425 cycles, which corresponds to $\omega_3 = 2\pi/7425 \approx 0.00085$ radians per second. Probability $P(x, t)$ (in blue) is constant over the entire episode.

For continuous space $\omega_n = (n + \frac{1}{2})\omega$. The value for ω can be derived from $x = \rho\xi$. With cell size a , also $\underline{x} = ax$ must hold. Hence,

$$\rho\xi = \rho\sqrt{\frac{m\omega}{\hbar}} = 1 \quad \text{and} \quad \omega = \frac{\hbar}{m\rho^2} = \frac{2\theta}{\rho^2}. \quad (3.19)$$

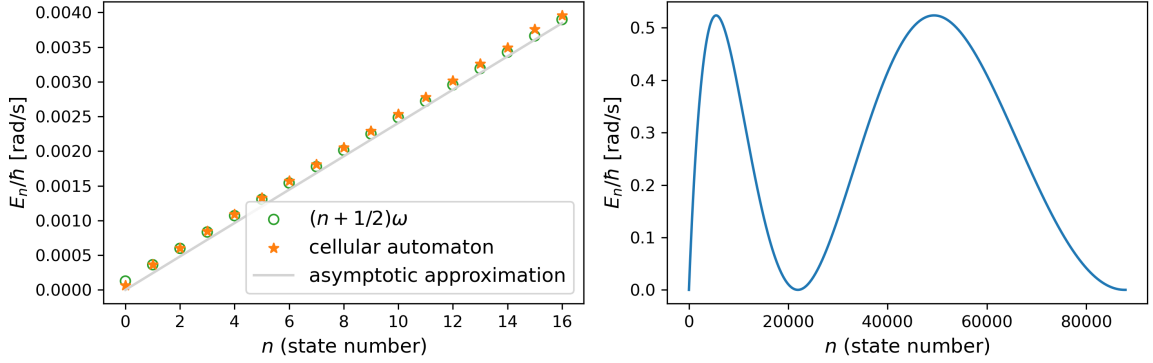


Figure 10: (left) The energy levels E_n/\hbar of the harmonic oscillator for $n \leq 16$. The orange *s show the measured frequencies ω_n of $\Psi_n(x, t)$ and the green circles show $(n + \frac{1}{2})\omega$. (right) The energy levels for large n , based on an asymptotic expansion of $H_n(\rho\xi)$.

Figure 10 (left) shows the energy levels $E_n/\hbar = \omega_n$ for $n \leq 16$. Each orange * is obtained by initializing the cellular automaton with ψ_n , and evolving the automaton until it returns to ψ_n . The energy level ω_n equal the reciprocal values of the measured time intervals. The thus obtained ω_n agree well with $\omega_n = (n + \frac{1}{2})\hbar\omega$.

To get an impression for the CSA behavior for large n , an asymptotic expansion of the Hermite polynomials can be used, e.g. based on [1], formula 13.6.38, parameters 13.5.16. Asymptotically, for $n \rightarrow \infty$, this expansion is of the form

$$A(n) \cos(\underline{x}\sqrt{2n} - \frac{n\pi}{2})B(n, \underline{x}) , \quad (3.20)$$

where $A(n)$ does not depend on \underline{x} and $B(n, \underline{x})$ has only two zeros in \underline{x} . This expansion suggests an “effective wave number” $k = \frac{1}{\rho}\sqrt{2n}$. It also implies that at the bottom of the $V(\underline{x})$ parabola there is a half cosine with $V(\underline{x}) \approx 0$. Application of the dispersion relation of the free particle⁵ (3.10) to the “effective” k cited above results in

$$\omega_n(\theta, \rho) \approx 4\theta \sin^2\left(\frac{1}{\rho}\sqrt{\frac{n}{2}}\right) + \frac{4}{3}\theta^3 \cos\left(\frac{1}{\rho}\sqrt{2n}\right) \sin^2\left(\frac{1}{\rho}\sqrt{2n}\right) + O(\theta^4) . \quad (3.21)$$

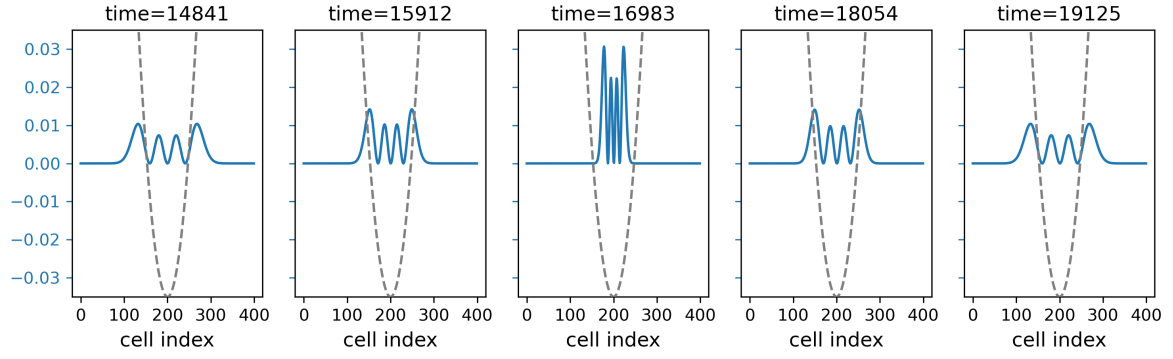
Figure 10 (right) shows $\omega_n(\theta, \rho)$ versus n for $\theta = \pi/24$ and $\rho = 400/12$. Its quasi periodic dependency on state number n is, again, an immediate consequence of the spatial aliasing resulting from the sampling of $W_{harmonic}$. For $n \leq 16$ these asymptotic levels are also depicted in gray in the (left) panel, where they agree well with the measured ω_n .

3.6 A time-dependent harmonic oscillator

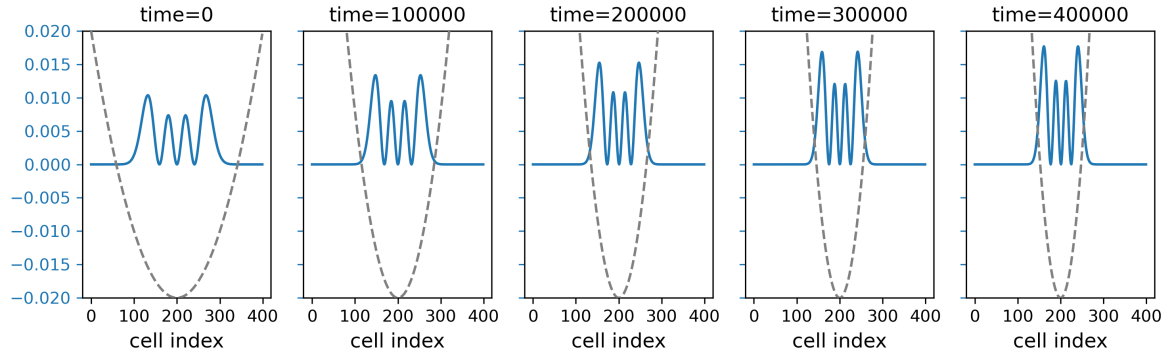
The harmonic oscillator of the previous subsection becomes time dependent with a time-dependent potential $V(x, t)$, as e.g. in

$$V(x, t) = s(t)V(x) \quad s(t) = \min(\max(1 + \alpha(t - t_s), 0), s_{max}) . \quad (3.22)$$

Slope $s(t)$ is 0 initially, and from t_s onwards increases by α per iteration until $s_{max} = 9$ is reached. In the experiment of Figure 11 the harmonic oscillator is initialized with the same state as in Figure 9 and $V(x, t)$ is updated every ten iterations.



(a) After an instantaneous increase the waveform quasi-periodically narrows and widens.



(b) During an adiabatic increase over 400,000 cycles the eigenstate gradually narrows.

Figure 11: The evolution of the harmonic oscillator for the $n=3$ eigen state in response to ninefold increase of the potential. (Note the difference in time frames.)

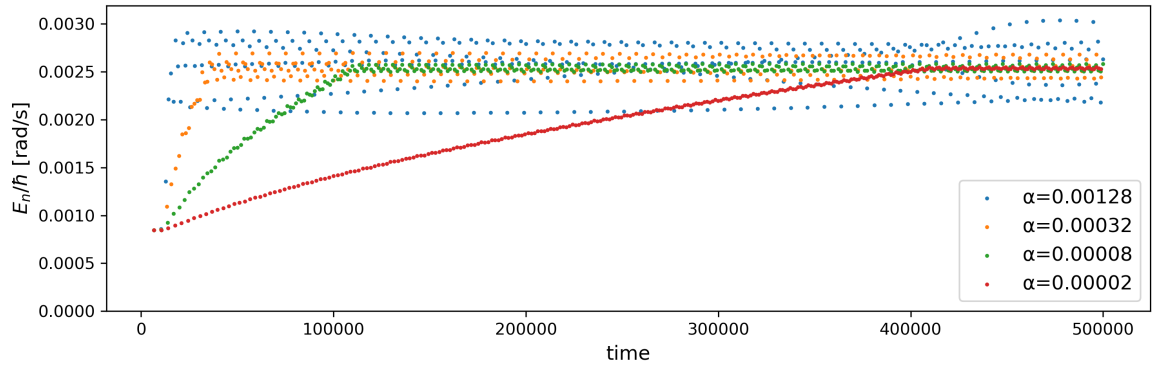


Figure 12: The energy levels E_n/\hbar of the harmonic oscillator for $n=3$ with $V(x, t)$ increasing over time. The red trajectory is marginally adiabatic; the eigen state evolves gradually. The green, orange, and blue ones are clearly diabatic, leading to squeezed states.

Figure 12 shows the energy levels $E_3(t)/\hbar = \omega(t)$ for four values of α , ranging from 0.00002

⁵While this ignores the potential $V(x)$ of the oscillator, it does highlight the effects of spatial aliasing.

to 0.00128. The colored markers are derived from $I(t)$,

$$I(t) = \sum_x |\text{Im}(\Psi(x, t))| . \quad (3.23)$$

For a time-independent Hamiltonian $I(t) = |\sin(\omega t + \phi)|$ for some ϕ . Then curve $I(t)$ touches zero periodically, with a fixed time interval π/ω . For a time-dependent Hamiltonian, the time intervals t_i between successive minima of $I(t)$ vary over time. The marker series of Figure 12, per α value, represent the series (T_i, ω_i) , where $\omega_i = \pi/t_i$ and $T_i = \sum_{j \leq i} t_j$.

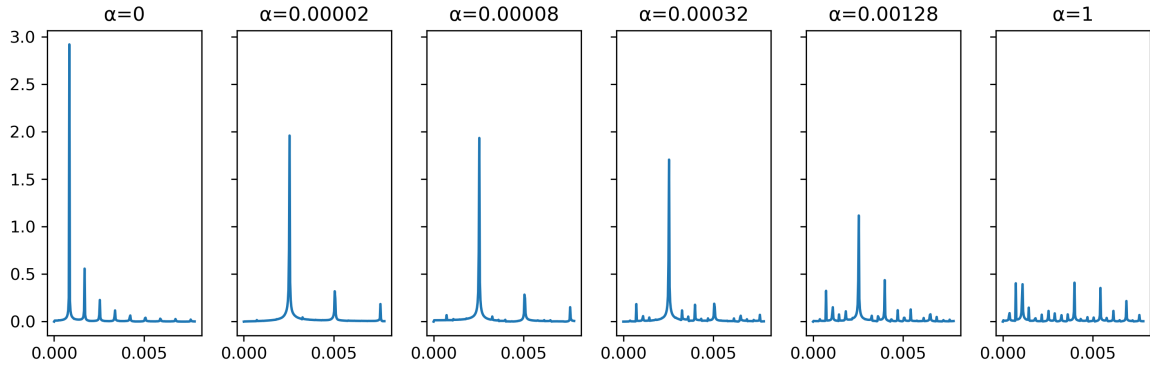


Figure 13: Frequency spectra of $I(t)$ for time interval $[400k, 500k]$ for various values of α .

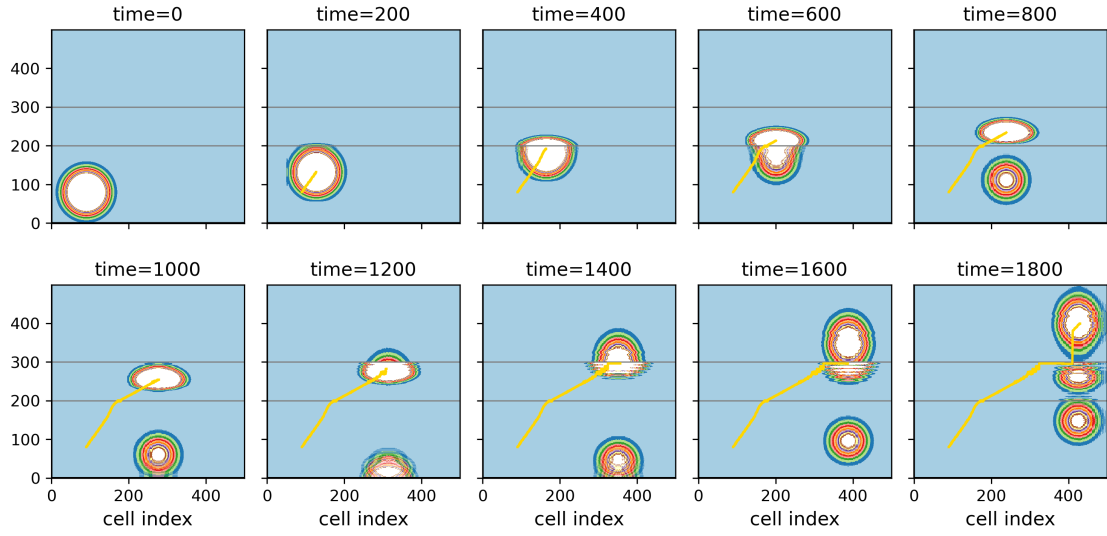
The time-dependent harmonic oscillator has been analyzed extensively, as, for example, in [28, 30], mostly with an emphasis on theory. Schrödinger cellular automata may offer a new tool to their study. For example, Figure 13 shows a low-frequent portion of the FFT transform of $I(t = [400k, 500k])$ for various values of α , after elimination of the DC component. For $\alpha=0$, the evolution is time independent, with a fundamental frequency $\omega=0.0008$ radians per second. This is consistent with the observed 7425 cycles in Figure 9. The higher harmonics are a byproduct of the absolute operation in the definition of $I(t)$ in (3.23). For the adiabatic evolution ($\alpha=0.00002$), the entire spectrum is essentially stretched by $3\times$, as to be expected. For higher values of α , the spectrum becomes increasingly polluted by components that are both higher *and lower* in frequency than the fundamental one. The spectrum for $\alpha=1$ is rather messy; the fundamental frequency is barely visible, and a proper detection of the minima of $I(t)$ appears infeasible.

4 Experiments with 2D Schrödinger cellular automata

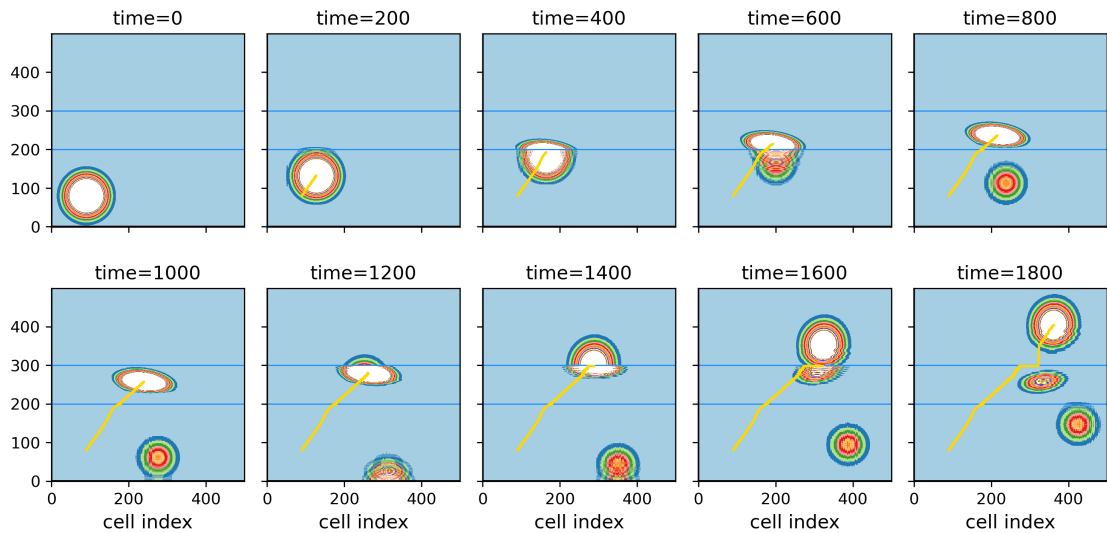
This section describes five experiments with 2D SCA. All SCA apply the same $\theta = \pi/24$, but differ in scalar potential $V(\mathbf{x})$, reflective surfaces $X(\mathbf{x})$, and/or vector potential $\mathbf{A}(\mathbf{x})$. The results are visualized as 2D color plots of $|\Psi|^2$ based on a *qualitative* colormap, in order to highlight the geometric features of the wave forms. The light blue backdrop implies a negligible $|\Psi|^2$ and white indicates a high value of $|\Psi|^2$.

4.1 Refraction

Refraction is the redirection of a wave as it passes from one medium to another. The refraction experiment of Figure 14a is a 2D version of the 1D refraction automaton of Figure 5b. The horizontal region in the middle has a potential $V_{rf} = 0.24\delta$. The 2D wave packet partially bounces off that region and partially propagates through that region at a reduced velocity. Subsequently, the reduced packet further splits into two parts, one escaping from the V region, and the other remaining inside. Note that the vertical component of the wave-packet velocity is affected, unlike the horizontal one.



(a) The region in the middle has a fixed potential $V_{rf} = 0.24\delta$.



(b) The region in the middle has a reduced value for θ : $\theta_{rf} = \pi/38$.

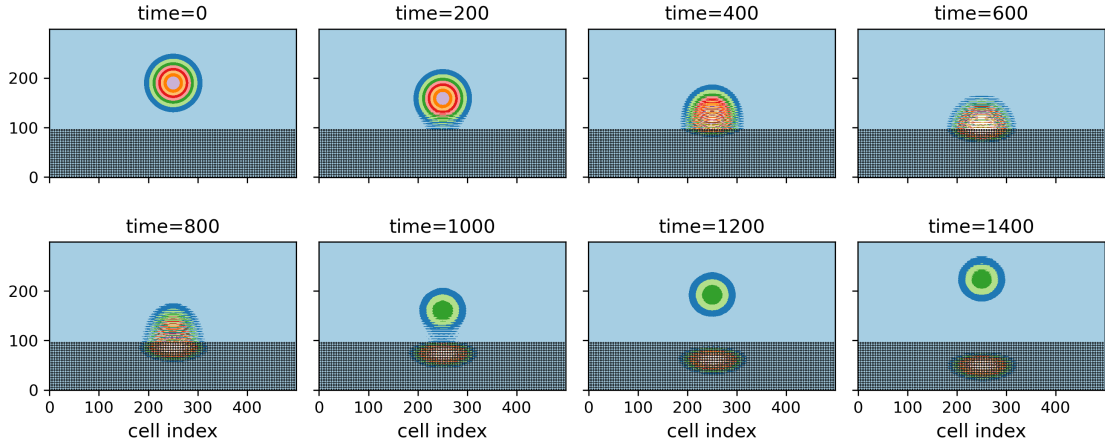
Figure 14: Two refraction experiments of a 2D Gaussian wave packet.

The inhomogeneous SCA of Figure 14b is similar, but now the middle region has a reduced

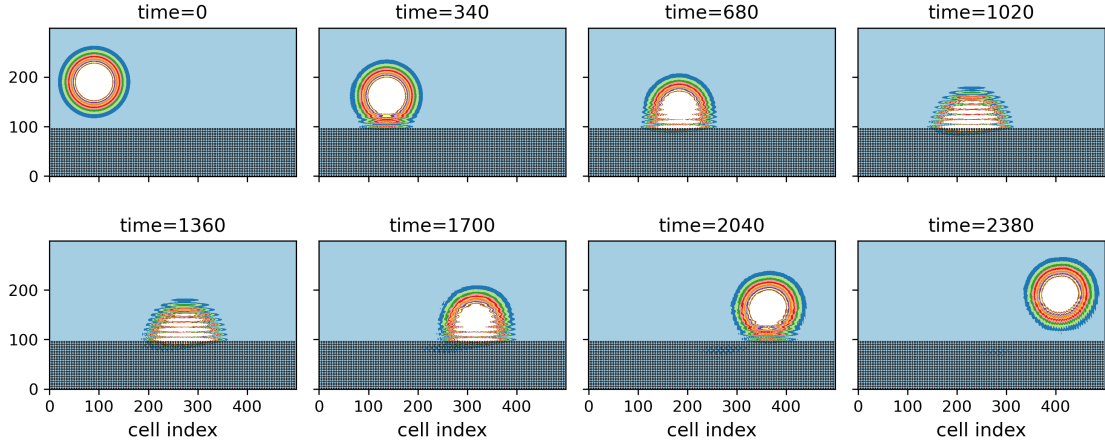
value for θ : $\theta_{rf} = \pi/38$. This results in a reduced group velocity in both x and y . Neither refraction experiment is consistent with Snell's law of refraction.

4.2 The Davisson-Germer experiment

The Davisson-Germer experiment [18] in 1927 confirmed the wave-particle duality hypothesis (de Broglie), and thereby the wave mechanics approach of the Schrödinger equation.



(a) With an angle of incidence of 90° the wave packet is mostly absorbed.



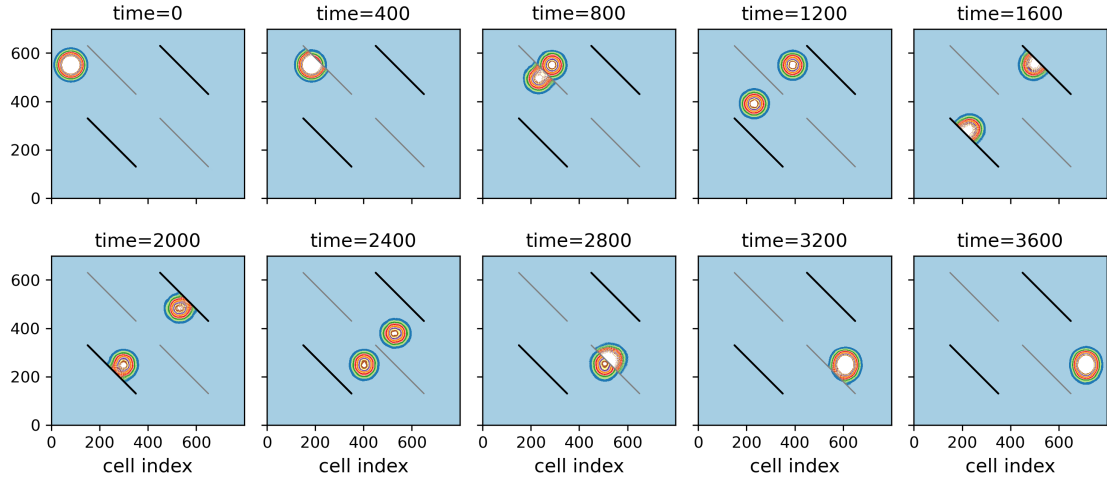
(b) With an angle of incidence of 30° the wave packet is almost entirely reflected.

Figure 15: The Davisson-Germer experiment.

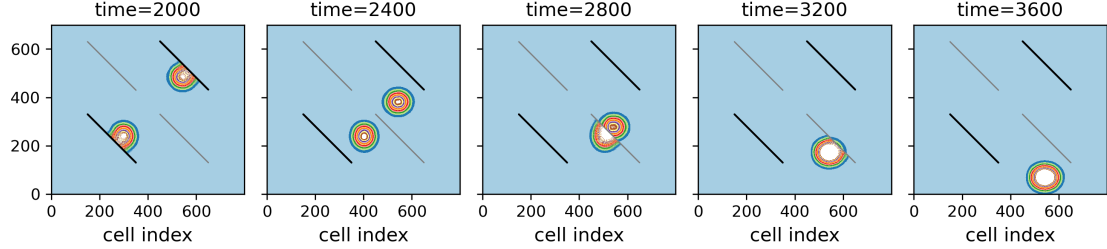
In Figure 15 the surface of the original crystal of nickel metal is modelled by a regular grid of single-cell reflectors (Subsection 2.5), spaced by five cells (half a wavelength) in each direction. Davisson and Germer fired slow-moving electrons at this crystalline nickel target and observed a diffraction pattern, where the reflected electron intensity depends on the angle of incidence. This diffraction can be fully explained in terms of interference, using Bragg's law. The SCA of Figure 15 visualizes such differences in diffraction for 90 and 30 degree angles of incidence of a wave packet.

4.3 A Mach-Zehnder interferometer

A Mach-Zehnder (MZ) interferometer is an instrument to measure phase-shift variations and was proposed by Ludwig Mach and Ludwig Zehnder in the late 19th century. Practical instruments are based on photons (collimated light), but early this century Ji et al [26] demonstrated a Mach-Zehnder interferometer based on electrons.



(a) The lengths of the top-right and left-bottom paths are equal.



(b) The lengths of the top-right and left-bottom paths differ by half a wavelength.

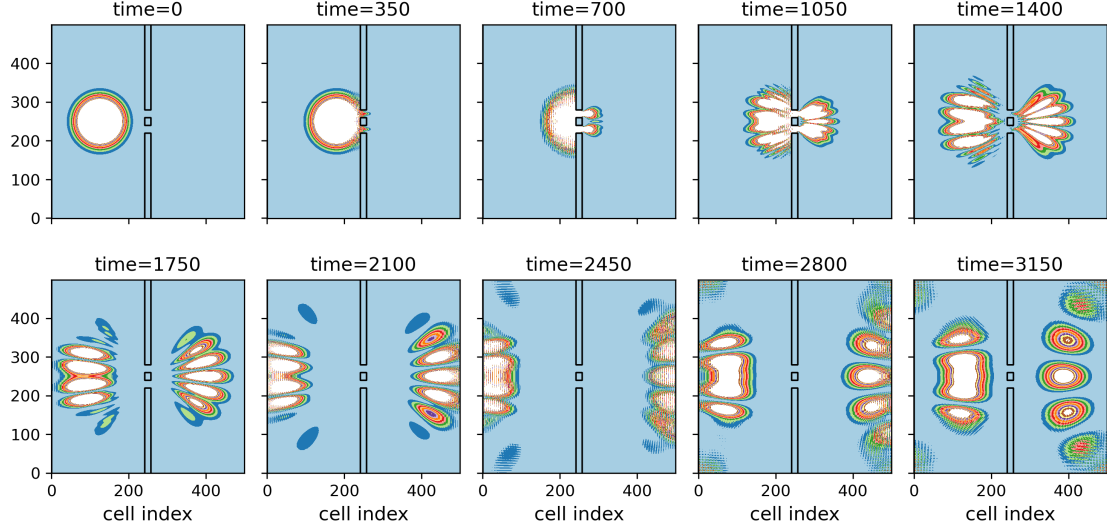
Figure 16: The Mach-Zehnder interferometer.

The prototypical MZ interferometer of Figure 16 consists of two mirrors (black) and two beamsplitters (gray), all placed under a 45 degree angles. The mirrors are reflective single-cell-width surfaces (Subsection 2.5), and the beam splitters are single-cell-width surfaces with a potential $V_{bs} = 0.248\delta$. The difference in outcomes (wave-packet exit directions) for Figures 16a and 16b stems from the respective path-lengths differences. The SCA evolutions nicely visualize that the MZ interferometer must be described by a genuine quantum superposition of the two wave-packet paths.

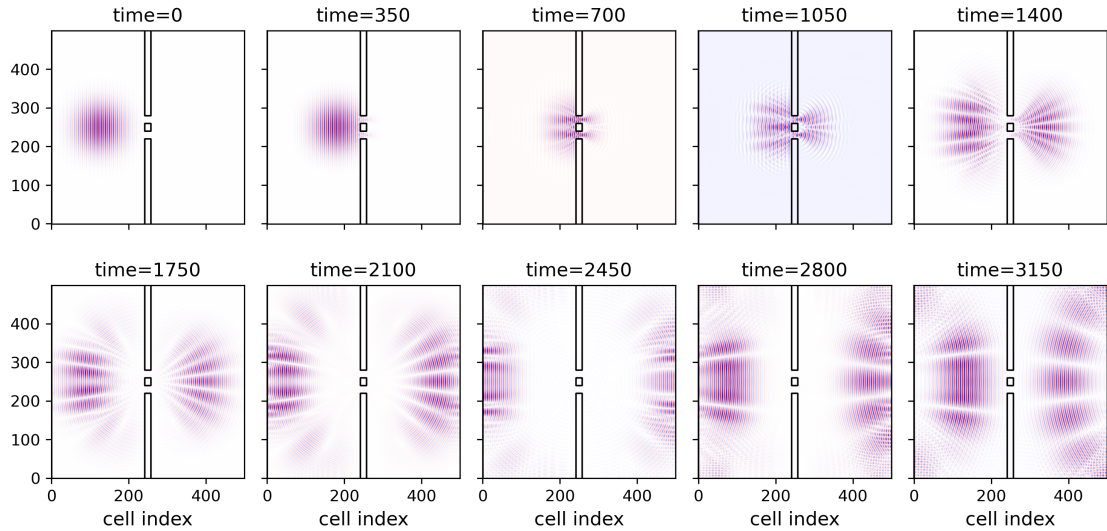
4.4 The double-slit experiment

The double-slit experiment demonstrates quantum interference of a single massive particle. Feynman describes this form of interference as *“a phenomenon which is impossible, absolutely impossible, to explain in any classical way, and which has in it the heart of quantum mechan-*

ics” [22]. Single-electron interference, using a biprism beam splitter, was demonstrated by Merli et al [32].



(a) Colors show different values of $|\Psi|^2$.



(b) The color red (blue) shows positive (negative) values of $\text{Re}(\Psi)$.

Figure 17: Double-slit diffraction.

The SCA of Figure 17 describes a vertical screen with two slits, each 20 cells wide (two wavelengths), separated by 40 cells (four wavelengths). The SCA evolves for well over 3000 cycles, showing interference patterns at both sides of the screen.

Figure 18 compares the observed diffraction pattern with those described by the Fraunhofer diffraction equation [44] for both narrow slits and wide slits:

$$I_{\text{narrow}}(\phi) \propto \cos^2\left(\frac{\pi d \sin \phi}{\lambda}\right), \quad I_{\text{wide}}(\phi) \propto \cos^2\left(\frac{\pi d \sin \phi}{\lambda}\right) \text{sinc}\left(\frac{\pi b \sin \phi}{\lambda}\right), \quad (4.1)$$

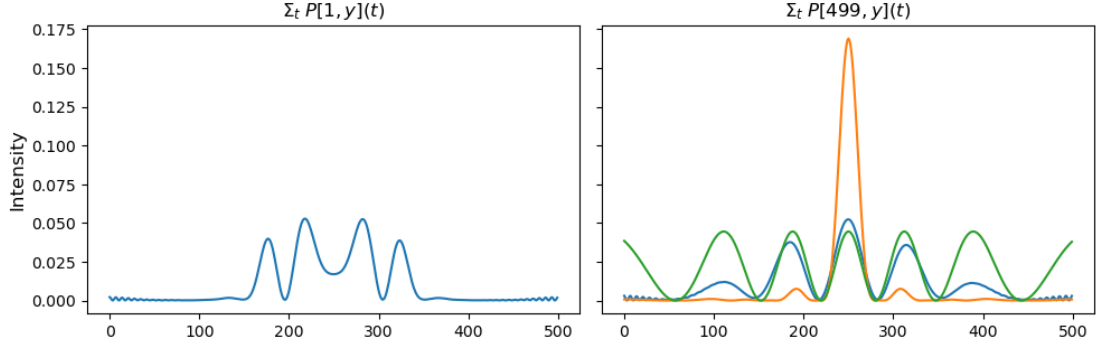


Figure 18: The observed double-slit diffraction pattern (blue) compared to those of the Fraunhofer diffraction equation for narrow slits (green) and for wide slits (orange).

where d is the slit separation, b the slit width, and ϕ the angle with respect to the mid- y horizontal. These intensities are normalized across the three central peaks. Apparently, the observed pattern with $b = 2\lambda$ lies somewhere in between. Note that the observed diffraction pattern stems from a single wave packet, whereas in a practical double-slit experiment a diffraction pattern emerges only after the detection of many independent particles.

The double-split experiments of Oliveira et al [35] describe quantum walks for various QW coins. Their Hadamard interference patterns shows a remarkable contrast. The interference pattern on the right-hand side of the screen is similar to that of Young's original experiment and to that of Figures 17 and 18-(right). The pattern on the left-hand side of the screen is distinctly unphysical, as if the probabilities tend to stick to the perimeter and the corners of the lattice. (No explanation is offered for this.)

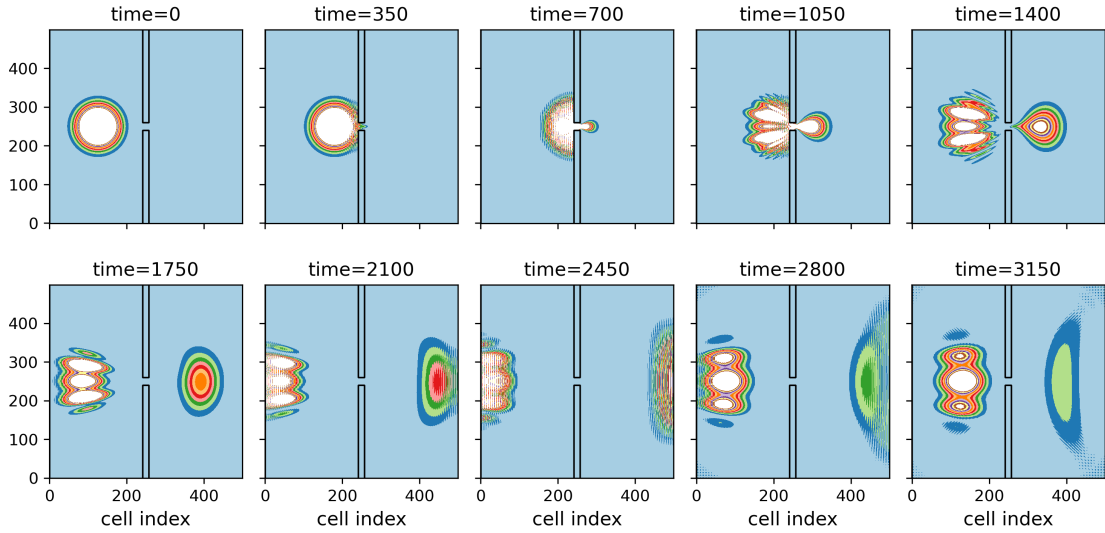
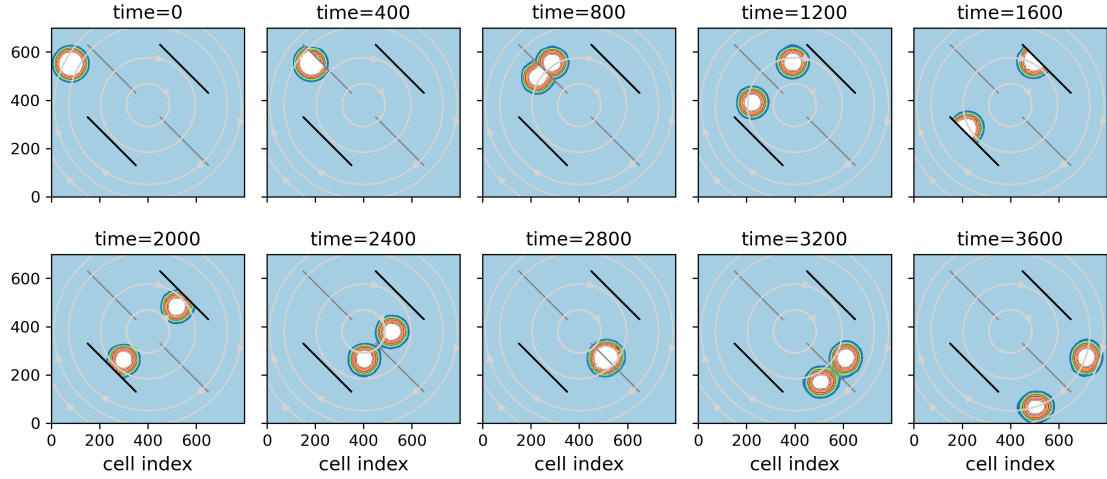


Figure 19: Single-slit diffraction: the reflections from the two screen halves interfere on the left-hand side of the screen.

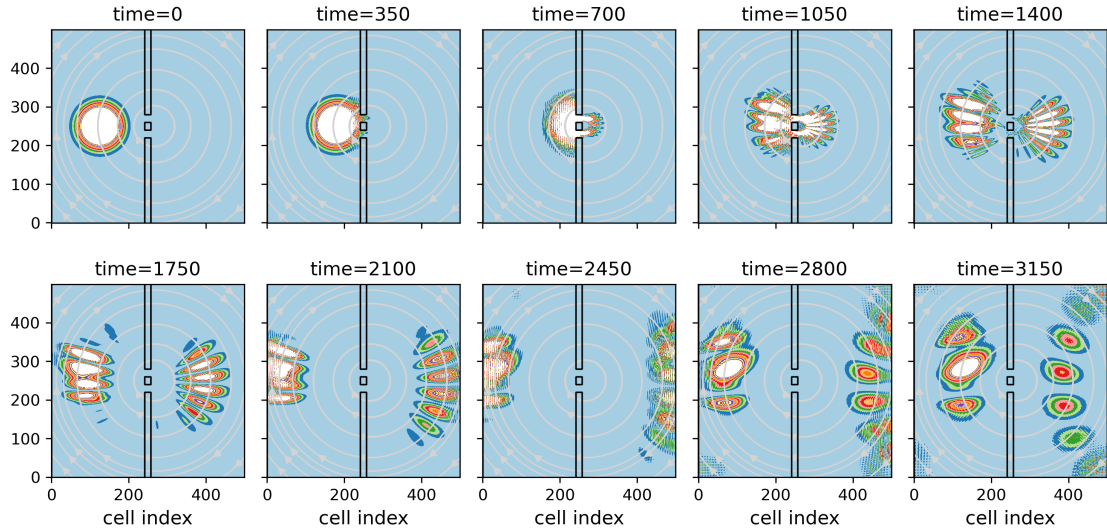
The SCA of Figure 19 describes a vertical screen with a single slit. Its evolution over about 3000 cycles shows an interference pattern only at the left-hand side of that screen, resulting from the reflections of the two screen halves.

4.5 The Aharonov-Bohm effect

The Aharonov–Bohm effect is a quantum-mechanical effect in which an electrically charged particle is affected by magnetic *potential* \mathbf{A} , despite being confined to a region in which magnetic *field* \mathbf{B} is zero. The effect was predicted by Aharonov and Bohm [2] and experimentally confirmed by Tonomura et al [41]. A good introduction is [22] Vol. II, 15-5.



(a) A solenoid is placed at the center of a Mach-Zehnder interferometer.



(b) A solenoid is placed just behind the screen center of a double-slit experiment.

Figure 20: The Aharonov-Bohm effect. The magnetic potential is shown by gray arrows.

The experiment of Figure 20a is a variation of that of Figure 16a, where a long solenoid is introduced at the center of a Mach-Zehnder interferometer, perpendicular to the plane. The magnetic potential of the solenoid is given by [22], Vol. II, 14-4

$$\mathbf{A}_{x'} = -K \frac{y'}{x'^2 + y'^2} \quad \mathbf{A}_{y'} = K \frac{x'}{x'^2 + y'^2} \quad \mathbf{A}_z = 0, \quad (4.2)$$

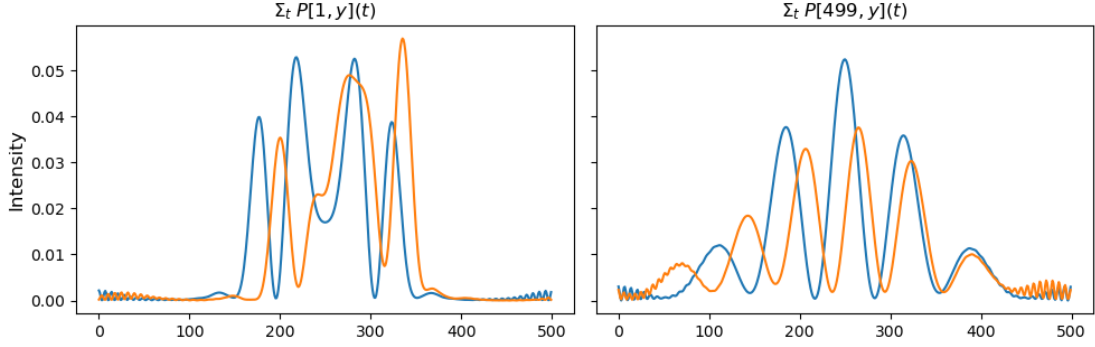


Figure 21: The blue curves show the original double-slit diffraction patterns of Figure 18. The orange curves show a shift to the right, due to the magnetic potential.

where K is some constant, and x' and y' are taken relative to the center of the solenoid. This potential is included in the evolution matrices \mathbf{U}_0 and \mathbf{U}_1 according to the split Hamiltonian of Subsection 2.4. The presence of this vector potential leads to a different experimental outcome (exit direction of the wave packet).

The experiment of Figure 20b is a variation of that of Figure 17, where the solenoid is introduced just behind the screen, between the two slits. Figure 21 shows that the presence of this potential leads to a right-shift of the diffraction patterns.

5 Conclusion

Schrödinger cellular automata can be derived from the Schrödinger equation as follows.

1. Discretize the continuous Schrödinger Hamiltonian and express it matrix form, \mathbf{H} .
2. Split the Hamiltonian matrix \mathbf{H} (recursively) into a sum of block-diagonal matrices, and express it in terms of Hermitian 2×2 matrices $\mathbf{B}_W(\mathbf{x})$ for $W \in \{X, Y, Z\}$.
3. Approximate $\exp(-i\tau/\hbar \mathbf{H})$ term by term (recursively), and express the resulting evolution matrix \mathbf{U} in terms of unitary 2×2 matrices $\mathbf{C}_W(\mathbf{x}) = \exp(-i\tau/\hbar \mathbf{B}_W(\mathbf{x}))$.

For the free particle this recipe leads to known block (Margolus) unitary cellular automata (Subsections 2.2 and 2.4), that are mathematically equivalent to a known class of staggered quantum walks. The recipe naturally extends to 3D inhomogeneous Hamiltonians (Subsection 2.4), with scalar potential $V(\mathbf{x})$ and vector potential $\mathbf{A}(\mathbf{x})$. Below the utility of SCAs is assessed from two perspectives: 1) as a tool for practical single-particle experiments and 2) as a formalism to address the “what if” question cited in the introduction.

As tool for analyzing and visualizing non-relativistic single-particle experiments, it is highly versatile, accurate, and computationally very efficient. SCA provide:

- full control over boundaries $X(\mathbf{x})$, scalar potential $V(\mathbf{x})$, vector potential $\mathbf{A}(\mathbf{x})$, and the initial state, all at cell granularity, with \mathbf{x} a position in 1, 2, or 3 dimensions,
- the option to evolve \mathbf{U} over time (a time-dependent Hamiltonian), and
- full observability at cell granularity at every time step.

All of these have been demonstrated by a rich set of experiments in Sections 3 and 4. The (systematic) approximation error in the involved physical quantities is $\mathcal{O}(\theta^3)$, and typically amounts to about 1%. Finally, the intrinsic sparsity of the evolution matrices $\mathbf{U}_0\mathbf{U}_1$ and $\mathbf{U}_1\mathbf{U}_0$ results in a very computationally efficient evolutions. The experiments of this paper typically take only a few minutes on a MacBook.

The introduction highlighted the “what if” question: *what if quantum dynamics occurs on a discrete lattice and in discrete time steps, e.g. at the Planck scale* [39, 23, 7, 10]? D’Ariano coined the phrase *Planck cell* [17], where the cell size a and time step τ correspond to the Planck length and the Planck time, with $c = a/\tau$. A wave packet with a wavelength $\lambda = 2a$ would have an energy $h\nu = \frac{1}{2}hc/a \approx 4 \cdot 10^{28} \text{eV}$. This value is many orders of magnitude beyond the 13.6 TeV of the LHC and the $\approx 3 \cdot 10^{20} \text{eV}$ of the most energetic cosmic-ray particles observed. This suggests that for “realistic” wave packets the wavelengths must exceed many thousands of cell sizes, outside the scope of the experiments of this study.

The most remarkable consequence of the discretization of space is that velocities become periodic in wavenumber k and energy levels similarly, as shown in various manifestations in Section 3. Likewise, evolution matrix \mathbf{U} becomes periodic in scalar potential $V(\mathbf{x})$, Subsection 2.5. This unavoidably connects quantum physics to the realm of Nyquist rates and spatial aliasing. These periodicity properties are not particular to SCA, but cellular automata offer an effective and efficient tool to analyze them. Further exploration of the “what if” question, towards relativistic velocities, suggests additional analysis and experiments with Dirac cellular automata [10].

References

- [1] M. Abramowitz and I. Stegun. *Handbook of Mathematical Functions*. Dover Publications, 1983.
- [2] Y. Aharonov and D. Bohm. Significance of electromagnetic potentials in the quantum theory. *Phys. Rev.*, 115:485–491, Aug 1959. DOI: [10.1103/PhysRev.115.485](https://doi.org/10.1103/PhysRev.115.485). URL <https://link.aps.org/doi/10.1103/PhysRev.115.485>.
- [3] Yakir Aharonov, Liema Davidovich, and N. Zagury. Quantum random walks. *Physical review. A*, 48:1687–1690, 09 1993. DOI: [10.1007/BFb0083545](https://doi.org/10.1007/BFb0083545).
- [4] Andris Ambainis, Julia Kempe, and Alexander Rivosh. Coins make quantum walks faster. In *Proceedings of the Sixteenth Annual ACM-SIAM Symposium on Discrete Algorithms*, SODA ’05, page 1099–1108, 2005. ISBN 0898715857.
- [5] Pablo Arnault and Fabrice Debbaesch. Landau levels for discrete-time quantum walks in artificial magnetic fields. *Physica A: Statistical Mechanics and its Applications*, 443: 179–191, 2016. ISSN 0378-4371. DOI: <https://doi.org/10.1016/j.physa.2015.08.011>. URL <https://www.sciencedirect.com/science/article/pii/S0378437115006664>.
- [6] P. Arrighi. An overview of quantum cellular automata. *Natural Computing*, 18(4):885–899, 2019. DOI: [10.1007/s11047-019-09762-6](https://doi.org/10.1007/s11047-019-09762-6). URL <https://doi.org/10.1007/s11047-019-09762-6>.
- [7] Pablo Arrighi, Vincent Nesme, and Marcelo Forets. The dirac equation as a quantum walk: higher dimensions, observational convergence. *Journal of Physics A: Mathematical and Theoretical*, 47(46):465302, nov 2014. DOI: [10.1088/1751-8113/47/46/465302](https://doi.org/10.1088/1751-8113/47/46/465302). URL <https://dx.doi.org/10.1088/1751-8113/47/46/465302>.

- [8] Iwo Bialynicki-Birula. Weyl, dirac, and maxwell equations on a lattice as unitary cellular automata. *Physical review D: Particles and fields*, 49:6920–6927, 07 1994. DOI: [10.1103/PhysRevD.49.6920](https://doi.org/10.1103/PhysRevD.49.6920).
- [9] Alessandro Bisio, Giacomo Mauro D’Ariano, and Alessandro Tosini. Dirac quantum cellular automaton in one dimension: *Zitterbewegung* and scattering from potential. *Phys. Rev. A*, 88:032301, Sep 2013. DOI: [10.1103/PhysRevA.88.032301](https://doi.org/10.1103/PhysRevA.88.032301). URL <https://link.aps.org/doi/10.1103/PhysRevA.88.032301>.
- [10] Alessandro Bisio, Giacomo Mauro D’Ariano, and Alessandro Tosini. Quantum field as a quantum cellular automaton: The dirac free evolution in one dimension. *Annals of Physics*, 354:244–264, 2015. ISSN 0003-4916. DOI: <https://doi.org/10.1016/j.aop.2014.12.016>. URL <https://www.sciencedirect.com/science/article/pii/S0003491614003546>.
- [11] Bruce M. Boghosian and Washington Taylor. Simulating quantum mechanics on a quantum computer. *Physica D: Nonlinear Phenomena*, 120(1):30–42, 1998. ISSN 0167-2789. DOI: [https://doi.org/10.1016/S0167-2789\(98\)00042-6](https://doi.org/10.1016/S0167-2789(98)00042-6). URL <https://www.sciencedirect.com/science/article/pii/S0167278998000426>. Proceedings of the Fourth Workshop on Physics and Consumption.
- [12] Luis A. Bru, Germán J. de Valcárcel, Giuseppe Di Molfetta, Armando Pérez, Eugenio Roldán, and Fernando Silva. Quantum walk on a cylinder. *Phys. Rev. A*, 94:032328, Sep 2016. DOI: [10.1103/PhysRevA.94.032328](https://doi.org/10.1103/PhysRevA.94.032328). URL <https://link.aps.org/doi/10.1103/PhysRevA.94.032328>.
- [13] C. Cedzich, T. Geib, A. H. Werner, and R. F. Werner. Quantum walks in external gauge fields. *Journal of Mathematical Physics*, 60(1):012107, 01 2019. ISSN 0022-2488. DOI: [10.1063/1.5054894](https://doi.org/10.1063/1.5054894). URL <https://doi.org/10.1063/1.5054894>.
- [14] Pedro C. S. Costa, Renato Portugal, and Fernando de Melo. Quantum walks via quantum cellular automata. *Quantum Information Processing*, 17(17:226), 2018.
- [15] Pedro C.S. Costa. Quantum-to-classical transition via quantum cellular automata. *Quantum Information Processing*, 20(7), 2021. ISSN 1573-1332. DOI: [10.1007/s11128-021-03175-0](https://doi.org/10.1007/s11128-021-03175-0). URL <http://dx.doi.org/10.1007/s11128-015-1149-z>.
- [16] J. Crank and P. Nicolson. A practical method for numerical evaluation of solutions of partial differential equations of the heat-conduction type. *Advances in Computational Math.*, 6:207–226, 1947. URL <https://api.semanticscholar.org/CorpusID:16676040>.
- [17] Giacomo Mauro D’Ariano. The quantum field as a quantum computer. *Physics Letters A*, 376(5):697–702, 2012. ISSN 0375-9601. DOI: <https://doi.org/10.1016/j.physleta.2011.12.021>. URL <https://www.sciencedirect.com/science/article/pii/S0375960111014836>.
- [18] C. Davisson and L. H. Germer. Diffraction of electrons by a crystal of nickel. *Phys. Rev.*, 30:705–740, Dec 1927. DOI: [10.1103/PhysRev.30.705](https://doi.org/10.1103/PhysRev.30.705). URL <https://link.aps.org/doi/10.1103/PhysRev.30.705>.
- [19] Giuseppe Di Molfetta, Marc Brachet, and Fabrice Debbasch. Quantum walks in artificial electric and gravitational fields. *Physica A: Statistical Mechanics and its Applications*, 397:157–168, 2014. ISSN 0378-4371. DOI: <https://doi.org/10.1016/j.physa.2013.11.036>. URL <https://www.sciencedirect.com/science/article/pii/S0378437113011059>.
- [20] Giacomo Mauro D’Ariano, Nicola Mosco, Paolo Perinotti, and Alessandro Tosini. Discrete time dirac quantum walk in 3+1 dimensions. *Entropy*, 18(6), 2016. ISSN 1099-4300. URL <https://www.mdpi.com/1099-4300/18/6/228>.

- [21] Terry Farrelly. A review of Quantum Cellular Automata. *Quantum*, 4:368, November 2020. ISSN 2521-327X. DOI: [10.22331/q-2020-11-30-368](https://doi.org/10.22331/q-2020-11-30-368). URL <https://doi.org/10.22331/q-2020-11-30-368>.
- [22] Richard P. Feynman, Robert B. Leighton, and Matthew Sands. *The Feynman lectures on physics: The Definitive Edition (Vol. 2 & 3)*. Pearson, 2009. ISBN 9788131721698. URL <http://www.worldcat.org/isbn/9788131721704>.
- [23] Gerard 't Hooft. *The Cellular Automaton Interpretation of Quantum Mechanics*. Springer, 2015.
- [24] David J. Griffiths and Darrell F. Schroeter. *Introduction to quantum mechanics*. Cambridge University Press, Cambridge ; New York, NY, third edition edition, 2018. ISBN 978-1-107-18963-8.
- [25] Gerhard Grössing and Anton Zeilinger. Quantum cellular automata. *Complex Syst.*, 2(2):197–208, apr 1988. ISSN 0891-2513.
- [26] Yang Ji, Yunchul Chung, D. Sprinzak, M. Heiblum, D. Mahalu, and Hadas Shtrikman. An electronic mach–zehnder interferometer. *Nature*, 422(6930):415–418, March 2003. ISSN 1476-4687. DOI: [10.1038/nature01503](https://doi.org/10.1038/nature01503). URL <http://dx.doi.org/10.1038/nature01503>.
- [27] Jolly, Nicolas and Di Molfetta, Giuseppe. Twisted quantum walks, generalised dirac equation and fermion doubling. *Eur. Phys. J. D*, 77(5):80, 2023. DOI: [10.1140/epjd/s10053-023-00659-9](https://doi.org/10.1140/epjd/s10053-023-00659-9). URL <https://doi.org/10.1140/epjd/s10053-023-00659-9>.
- [28] T. Kiss, J. Janszky, and P. Adam. Time evolution of harmonic oscillators with time-dependent parameters: A step-function approximation. *Phys. Rev. A*, 49:4935–4942, Jun 1994. DOI: [10.1103/PhysRevA.49.4935](https://doi.org/10.1103/PhysRevA.49.4935). URL <https://link.aps.org/doi/10.1103/PhysRevA.49.4935>.
- [29] Iván Márquez-Martín, Pablo Arnault, Di Molfetta Giuseppe, and Armando Pérez. Electromagnetic lattice gauge invariance in two-dimensional discrete-time quantum walks. *Physical Review A*, 98(3):032333, September 2018. DOI: [10.1103/PhysRevA.98.032333](https://doi.org/10.1103/PhysRevA.98.032333). URL <https://amu.hal.science/hal-03594739>.
- [30] Daniel Martínez-Tibaduiza, Luis Pires, and Carlos Farina. Time-dependent quantum harmonic oscillator: a continuous route from adiabatic to sudden changes. *Journal of Physics B: Atomic, Molecular and Optical Physics*, 54(20):205401, nov 2021. DOI: [10.1088/1361-6455/ac36ba](https://doi.org/10.1088/1361-6455/ac36ba). URL <https://dx.doi.org/10.1088/1361-6455/ac36ba>.
- [31] Mena, A. Solving the 2D Schrödinger equation using the Crank-Nicolson method. <https://artmenlope.github.io/solving-the-2d-schrodinger-equation-using-the-crank-nicolson-method/>, 2023. [Online; accessed 23-Mar-2024].
- [32] P. G. Merli, G. F. Missiroli, and G. Pozzi. On the statistical aspect of electron interference phenomena. *American Journal of Physics*, 44(3):306–307, March 1976. DOI: [10.1119/1.10184](https://doi.org/10.1119/1.10184).
- [33] David A. Meyer. From quantum cellular automata to quantum lattice gases. *Journal of Statistical Physics*, 85(5–6):551–574, December 1996. ISSN 1572-9613. DOI: [10.1007/bf02199356](https://doi.org/10.1007/bf02199356). URL <http://dx.doi.org/10.1007/BF02199356>.
- [34] Mauro E. S. Morales, Pedro C. S. Costa, Giacomo Pantaleoni, Daniel K. Burgarth, Yuval R. Sanders, and Dominic W. Berry. Greatly improved higher-order product formulae for quantum simulation, 2024. URL <https://arxiv.org/abs/2210.15817>.
- [35] Amanda C. Oliveira, Renato Portugal, and Raul Donangelo. Simulation of the single- and double-slit experiments with quantum walkers, 2007. URL <https://arxiv.org/abs/0706.3181>.

- [36] R. Portugal, R. A. M. Santos, T. D. Fernandes, and D. N. Gonçalves. The staggered quantum walk model. *Quantum Information Processing*, 15(1):85–101, October 2015. ISSN 1573-1332. DOI: [10.1007/s11128-015-1149-z](https://doi.org/10.1007/s11128-015-1149-z). URL <http://dx.doi.org/10.1007/s11128-015-1149-z>.
- [37] A. T. Sornborger and E. D. Stewart. Higher-order methods for simulations on quantum computers. *Phys. Rev. A*, 60:1956–1965, Sep 1999. DOI: [10.1103/PhysRevA.60.1956](https://doi.org/10.1103/PhysRevA.60.1956). URL <https://link.aps.org/doi/10.1103/PhysRevA.60.1956>.
- [38] Frederick W. Strauch. Connecting the discrete- and continuous-time quantum walks. *Phys. Rev. A*, 74:030301, Sep 2006. DOI: [10.1103/PhysRevA.74.030301](https://doi.org/10.1103/PhysRevA.74.030301). URL <https://link.aps.org/doi/10.1103/PhysRevA.74.030301>.
- [39] Gerard 't Hooft. Quantization of discrete deterministic theories by hilbert space extension. *Nuclear Physics B*, 342(3):471—485, 1990.
- [40] Toffoli, Tommaso and Margolus, Norman. *Cellular Automata Machines: A New Environment for Modeling*. MIT Press, 04 1987. ISBN 978-0-262-20060-8. DOI: [10.7551/mitpress/1763.001.0001](https://doi.org/10.7551/mitpress/1763.001.0001).
- [41] Akira Tonomura, Tsuyoshi Matsuda, Ryo Suzuki, Akira Fukuhara, Nobuyuki Osakabe, Hiroshi Umezaki, Junji Endo, Kohsei Shinagawa, Yutaka Sugita, and Hideo Fujiwara. Observation of aharonov-bohm effect by electron holography. *Phys. Rev. Lett.*, 48:1443–1446, May 1982. DOI: [10.1103/PhysRevLett.48.1443](https://doi.org/10.1103/PhysRevLett.48.1443). URL <https://link.aps.org/doi/10.1103/PhysRevLett.48.1443>.
- [42] Kees van Berkel. UCAlab. <https://github.com/kees-van-berkel/UCAlab>, 2025.
- [43] Kees van Berkel, Jan de Graaf, and Kees van Hee. Experiments with Schrodinger Cellular Automata. <https://www.youtube.com/watch?v=tDi0HPf98ic>, 2025.
- [44] Wikipedia contributors. Fraunhofer diffraction equation, 2025. URL https://en.wikipedia.org/wiki/Fraunhofer_diffraction_equation. [Online; accessed 27-Jan-2025].